

Stirring in massive, young debris discs from spatially resolved Herschel images^{*}

A. Moór¹†, Á. Kóspál^{1,2}, P. Ábrahám¹, D. Apai³, Z. Balog⁴, C. Grady⁵, Th. Henning⁴, A. Juhász⁶, Cs. Kiss¹, A. V. Krivov⁷, N. Pawellek⁷ and Gy. M. Szabó^{1,8}

¹*Konkoly Observatory, Research Centre for Astronomy and Earth Sciences, Hungarian Academy of Sciences, PO Box 67, H-1525 Budapest, Hungary*

²*European Space Agency (ESA-ESTEC, SRE-S), P.O. Box 299, 2200 AG, Noordwijk, The Netherlands; ESA fellow.*

³*Department of Astronomy and Department of Planetary Sciences, The University of Arizona, Tucson, AZ 85721 USA*

⁴*Max-Planck-Institut für Astronomie, Königstuhl 17, 69117 Heidelberg, Germany*

⁵*Exoplanets and Stellar Astrophysics Laboratory, Code 667, Goddard Space Flight Center, Greenbelt, MD 20771 USA*

⁶*Leiden Observatory, Leiden University, Niels Bohrweg 2, NL-2333 CA Leiden, The Netherlands*

⁷*Astrophysikalisches Institut und Universitätssternwarte, Friedrich-Schiller-Universität Jena, Schillergäßchen 2–3, 07745 Jena, Germany*

⁸*ELTE, Gothard Astrophysical Observatory, H-9704 Szombathely, Szent Imre herceg út 112, Hungary*

Accepted ... Received ...; in original form ...

ABSTRACT

A significant fraction of main-sequence stars are encircled by dusty debris discs, where the short-lived dust particles are replenished through collisions between planetesimals. Most destructive collisions occur when the orbits of smaller bodies are dynamically stirred up, either by the gravitational effect of locally formed Pluto-sized planetesimals (self-stirring scenario), or via secular perturbation caused by an inner giant planet (planetary stirring). The relative importance of these scenarios in debris systems is unknown. Here we present new *Herschel Space Observatory* imagery of 11 discs selected from the most massive and extended known debris systems. All discs were found to be extended at far-infrared wavelengths, five of them being resolved for the first time. We evaluated the feasibility of the self-stirring scenario by comparing the measured disc sizes with the predictions of the model calculated for the ages of our targets. We concluded that the self-stirring explanation works for seven discs. However, in four cases, the predicted pace of outward propagation of the stirring front, assuming reasonable initial disc masses, was far too low to explain the radial extent of the cold dust. Therefore, for HD 9672, HD 16743, HD 21997, and HD 95086, another explanation is needed. We performed a similar analysis for β Pic and HR 8799, reaching the same conclusion. We argue that planetary stirring is a promising possibility to explain the disk properties in these systems. In HR 8799 and HD 95086 we may already know the potential perturber, since their known outer giant planets could be responsible for the stirring process. Interestingly, the discs around HD 9672, HD 21997, and β Pic are also unique in harbouring detectable amount of molecular CO gas. Our study demonstrates that among the largest and most massive debris discs self-stirring may not be the only active scenario, and potentially planetary stirring is responsible for destructive collisions and debris dust production in a number of systems.

Key words: stars: circumstellar matter – stars:individual: HD 9672, HD 10939, HD 16743, HD 17848, HD 21997, HD 50571, HD 95086, HD 161868, HD 170773, HD 182681, HD 195627 – infrared: stars

1 INTRODUCTION

Many main-sequence stars host circumstellar dust discs whose particles re-emit the absorbed stellar light and produce thermal emission at infrared (IR) and millimeter wavelengths. Grain-grain collisions and dynamical interactions

^{*} This work is based on observations made with the Herschel Space Observatory. Herschel is an ESA space observatory with science instruments provided by European-led Principal Investigator consortia and with important participation from NASA.
† E-mail: moor@konkoly.hu

with the stellar radiation lead to the removal of the emitting dust particles on a timescale significantly shorter than the age of the star. It is believed that the particles are continuously replenished by collisional erosion of previously formed larger bodies. Thus, these *debris* discs are composed of second generation material, and their presence implies the existence of a significant planetesimal population. Because of the close link between the dust and large bodies the detailed investigation of the debris discs can also provide information on the characteristics and evolution of the parent planetesimal belt(s) and even on the formation and evolution of the underlying planetary system (e.g. Wyatt 2008).

For collisions to produce a copious amount of dust, the relative velocities between the colliding larger bodies must exceed a critical value. This requires a dynamical stirring of the planetesimals' motion. In the *self-stirring* scenario proposed by Kenyon & Bromley (2004), the gradual build-up of large planetesimals via collisional coagulation of smaller bodies eventually leads to an enhanced dust production. According to this model, the emergent largest planetesimals ("oligarchs") perturb the orbits of neighbouring smaller bodies, increasing their inclination and eccentricities. This results in destructive collisions and initiates a collisional cascade. In a specific disc region the peak dust production roughly coincides with the formation of ~ 1000 km radius (\sim Pluto-sized) planetesimals. Alternatively, in the *planetary or binary stirring* scenario (Wyatt 2005b; Mustill & Wyatt 2009), a giant planet or a stellar companion triggers the collisions. In this case, the companion can dynamically excite the motion of planetesimals via secular perturbations even if the companion is located far from the planetesimals. Self-stirring is an inside-out process, i.e. the collisional cascade is ignited in the inner disc first and then the active dust production propagates outward. The same is true for planetary stirring if the perturber is located closer to the star than the planetesimal belt. *Stellar flybys* can also initiate more energetic collisions between planetesimals (Kenyon & Bromley 2002). The scarcity of stellar encounters among old field stars, however, suggests that this mechanism is likely limited to debris systems located in dense young clusters (Matthews et al. 2014b).

Very little is known about the relative contributions of self-stirring and planetary stirring in observed debris systems. Kennedy & Wyatt (2010) concluded that the observational statistics provided by the *Spitzer Space Telescope* (hereafter *Spitzer*) for debris discs around A-type stars can be reproduced by simulating the evolution of a sample of discs assuming either self-stirring or planetary stirring. Although the importance of the different mechanisms cannot be established by studying the whole debris population, there are some individual systems where self-stirring can be excluded with high probability. In self-stirring models, the pace of the outward propagation of the formation of 1000 km-sized planetesimals depends on the disc mass: the more massive the disc initially, the faster the outwards spread. Therefore, the existence of dust-producing planetesimals at large stellocentric radii around a relatively young star would require an unrealistically massive initial protoplanetary disc. In these cases, planetary stirring by an inner planet is a natural candidate because its timescale in the outer disc could be faster than that of the growth of large planetesimals needed for self-stirring. Indeed, based

on this consideration, Mustill & Wyatt (2009) identified debris discs around two young moving group members where self-stirring is unlikely.

The location of the dust grains in a debris disc is generally estimated from their temperature and the star's luminosity, assuming thermal equilibrium. However, the temperature of a dust grain depends not only on its distance from the star, but also on its size and optical properties. Because of this well known degeneracy (e.g. Krivov 2010), modeling of the spectral energy distribution (SED) cannot provide an unambiguous picture on the spatial distribution of dust in debris systems. To break this degeneracy and to estimate the location of the emitting grains reliably and precisely, spatially resolved images are needed. Due to the unprecedented spatial resolution (6–11") and sensitivity of the *Herschel Space Observatory* (hereafter *Herschel*, Pilbratt et al. 2010) at far-infrared (far-IR) wavelengths, the number of resolved debris discs increased significantly in the last few years (Matthews et al. 2014b; Pawellek et al. 2014). These studies showed that disc sizes derived from resolved images are generally 2–4 times larger than those inferred from SED analysis assuming blackbody grains (e.g. Marshall et al. 2011; Booth et al. 2013; Morales et al. 2013).

Here we report on our *Herschel* observations of 11 debris discs, where young age and an earlier estimate of disc size from previous infrared observations hinted for stirring mechanisms other than self-stirring. We first review the target selection, observations, and data reduction aspects of the programme (Sect 2). In Sect 3 we summarize the stellar properties, present a basic analysis of the *Herschel* images and measure fluxes. We then compile and model the SED of the targets and model the resolved images using a simple geometrical approach (Sect. 4). The results are discussed in Sect. 5. Our conclusions are presented in Sect. 6.

2 OBSERVATIONS AND DATA REDUCTION

2.1 Sample selection

Nine of our targets were selected on the basis of their previous *Spitzer*/MIPS observations. By analysing *Spitzer* data of 27 debris systems around F-type stars we already identified two objects, HD 50571 and HD 170773, whose dust emission were marginally extended in 70 μ m MIPS images (Moór et al. 2011a). In order to search for further candidates we queried the *Spitzer* archive for bright debris systems (with flux density > 200 mJy at 70 μ m) located within 120 pc, and downloaded their MIPS 70 μ m observations. Using the same method as in Moór et al. (2011a) we found several additional marginally extended discs and estimated their characteristic sizes. We assumed that the derived sizes correspond to the size of the dust ring and that they are collocated with the parent planetesimals. Then, by adopting age estimates from the literature for each system, we evaluated the feasibility of the self-stirring mechanism for each disc based on the formulae from Mustill & Wyatt (2009). Selecting only those objects not yet included in other *Herschel* programmes, we identified nine discs (including HD 50571 and HD 170773), where self-stirring would require initial disc masses either at the extreme upper end of the mass distribution of protoplanetary discs obtained from millimetre

Table 1. Observation log

TARGET	INSTR./FILTER	OBS. ID	DATE
HD 9672	PACS 70/160	1342224377/1342224378	2011-07-18
HD 9672	PACS 100/160	1342224379/1342224380	2011-07-18
HD 9672	SPIRE	1342236226	2012-01-02
HD 10939	PACS 70/160	1342225326/1342225327	2011-07-23
HD 10939	PACS 100/160	1342225328/1342225329	2011-07-23
HD 10939	SPIRE	1342236211	2012-01-02
HD 16743	PACS 70/160	1342261271/1342261272	2013-01-17
HD 16743	SPIRE	1342268403	2013-03-25
HD 17848	PACS 70/160	1342225120/1342225121	2011-08-01
HD 17848	PACS 100/160	1342225122/1342225123	2011-08-02
HD 17848	SPIRE	1342230802	2011-10-11
HD 21997	PACS 70/160	1342237454/1342237455	2012-01-13
HD 21997	PACS 100/160	1342237456/1342237457	2012-01-13
HD 21997	SPIRE	1342238289	2012-01-28
HD 50571	PACS 70/160	1342233376/1342233377	2011-12-01
HD 50571	PACS 100/160	1342233378/1342233379	2011-12-01
HD 50571	SPIRE	1342226639	2011-08-16
HD 95086	PACS 70/160	1342225005/1342225006	2011-08-01
HD 95086	PACS 100/160	1342225007/1342225008	2011-08-01
HD 95086	SPIRE	1342226634	2011-08-16
HD 161868	PACS 70/160	1342231117/1342231118	2011-10-18
HD 161868	PACS 100/160	1342231119/1342231120	2011-10-18
HD 161868	SPIRE	1342229577	2011-09-23
HD 170773	PACS 70/160	1342241398/1342241399	2012-03-14
HD 170773	PACS 100/160	1342241400/1342241401	2012-03-14
HD 170773	SPIRE	1342216001	2011-03-13
HD 182681	PACS 70/160	1342231927/1342231928	2011-11-05
HD 182681	PACS 100/160	1342231929/1342231930	2011-11-05
HD 182681	SPIRE	1342230820	2011-10-11
HD 195627	PACS 70/160	1342232492/1342232493	2011-11-18
HD 195627	PACS 100/160	1342232494/1342232495	2011-11-19
HD 195627	SPIRE	1342216008	2011-03-13

measurements, or so high that the disc would be gravitationally unstable. These 9 objects are our prime candidates where alternative stirring mechanisms may operate. To this sample we added HD 16743 and HD 182681, where disc sizes inferred from our SED analysis of a sample of debris systems turned out to be unusually large.

The uncertainty of the disc sizes derived from the *Spitzer*/MIPS profiles turned out to be too high to confidently exclude the self-stirring scenario. New higher spatial resolution *Herschel* observations are indispensable to measure disc sizes with the required accuracy.

2.2 Herschel measurements

We obtained far-IR and submillimetre maps for our targets using the Photodetector Array Camera and Spectrometer (PACS, Poglitsch et al. 2010) and the Spectral and Photometric Imaging Receiver (SPIRE, Griffin et al. 2010) onboard the *Herschel Space Observatory*. Apart from HD 16743, which was observed as part of the OT1_ckiss.1 programme (PI: Cs. Kiss), all other maps were obtained in the framework of OT1_pabraham.2 (PI: P. Ábrahám). Table 1 presents the log of our *Herschel* observations.

2.2.1 PACS observations and data reduction

PACS data were obtained in mini scan-map mode (PACS Observer’s Manual v2.5¹) at a medium scan speed of 20'' s⁻¹, with 10 scan-legs of 3' length separated by 4''. For

¹ http://herschel.esac.esa.int/Docs/PACS/html/pacs_om.html

targets in the OT1_pabraham.2 programme we made maps with scan angles of 70° and 110° both in the 70 μm and in the 100 μm bands, repeated four times in each scan direction. This setup provided in total 8 separate scans both at 70 and 100 μm. Since every PACS observation provides a 160 μm measurement as well, at this wavelength we obtained in total 16 separate scans for our targets. In the case of HD 16743 only 100 μm and 160 μm maps were taken with a single repetition. With the medium scan speed the PACS beam size is ~5''.6, ~6''.8 and ~11''.4, at 70, 100 and 160 μm, respectively.

The PACS raw data were reduced with the Herschel Interactive Processing Environment (HIPE, Ott 2010) version 11.1 using PACS calibration file release version 56 and the standard HIPE scripts. We selected those data frames where the actual scan speed of the spacecraft was between 15 and 25'' s⁻¹. PACS maps are subject to 1/f noise that was removed by applying highpass filtering with filter widths of 25, 30, and 40 frames for the 70, 100, and 160 μm data, respectively. At a scan speed of 20'' s⁻¹ and with 10 Hz data sampling, these frame numbers correspond to filter widths of 102'', 122'' and 162'' in the 70, 100, and 160 μm bands. In order to avoid flux loss caused by this process, the immediate vicinity of our targets was excluded from the filtering using a circular mask placed at the sources’ positions. The mask radius was 25'' in the case of the 70 and 100 μm maps, and 30'' at 160 μm. The best filter widths and source mask radii were determined by processing the maps with different parameter values and measuring the target flux with aperture photometry. By increasing the filter width, the measured flux increased until a point where the flux no longer changed, pinpointing the filtering parameters where flux loss can be neglected. Glitches were identified and removed using the second-level deglitching HIPE task.

As a final step of reduction, we compiled individual scan maps (corresponding to the individual repetitions) with pixel sizes of 1''.1, 1''.4, and 2''.1 at 70, 100, and 160 μm using the 'PHOTPROJECT' task. Mosaics were also created in each band, by combining the individual scan maps using a weighted average.

In order to ensure that we did not filter out low level extended emission from the outer regions of the discs, the maps were also processed using the JScanam tool which is a Java and Jython based implementation of the Scanamorphos code (Roussel 2013) integrated in HIPE. Application of this algorithm with the "galactic" option ensures the preservation of extended emission at all scales. By comparing the JScanam maps with the previous ones we found that the radial profiles of our sources were identical in the two data sets and the new maps did not reveal additional faint extended emission around our sources. For the further analysis we always use the original high-pass filter maps.

2.2.2 SPIRE observations and data reduction

All SPIRE observations were obtained in Small Scan Map mode (see Spire Handbook v2.5²) resulting in simultaneous 250, 350, and 500 μm maps. We made two repetitions of the small maps for each target. Data were reduced with HIPE

² http://herschel.esac.esa.int/Docs/SPIRE/spire_handbook.pdf

v11.1 following the standard pipeline processing steps. The final maps were produced using the 'NAIVEMAPPER' task. The beam sizes were $\sim 17''.6$, $\sim 23''.9$, and $\sim 35''.2$ at 250, 350, and 500 μm , respectively, and the maps were resampled to pixel sizes of $6''$, $10''$, and $14''$ at these wavelengths.

2.3 Spitzer archival data

Apart from HD 182681, all of our targets were observed both with the Multiband Imaging Photometer for Spitzer (MIPS, Rieke et al. 2004) and the Infrared Spectrograph (IRS, Houck et al. 2004) onboard the *Spitzer Space Telescope* (Werner et al. 2004). All data were downloaded from the *Spitzer Heritage Archive*³.

MIPS observations were performed at 24 and 70 μm . In the case of HD 16743, HD 50571, and HD 170773, 160 μm maps are available as well. We downloaded all 70 μm MIPS data that were obtained in photometric imaging mode (default scale, small-field size). The basic calibrated data, produced by the pipeline version 18.12, were processed with the MOsacking and Point source Extraction (Makovoz & Marleau 2005, MOPEX) tool performing the same steps as described in Moór et al. (2011a). The final mosaic images had $4''$ pixels.

IRS observations of HD 21997 and HD 95086 were performed in Spectral Mapping mode, their spectra were taken from the literature (Moór et al. 2013a,b). For the other targets, where the IRS Staring Mode was used in the observations, the spectra were retrieved from the CASSIS⁴ database (Lebouteiller et al. 2011). As post-processing, we discarded outliers by fitting polynomials to the data of individual IRS modules using a robust method and then searching for data points outlying by more than 4σ from these fits. The longest wavelength parts of the LL1 and SL1 modules at wavelength $>38 \mu\text{m}$ and $>14.5 \mu\text{m}$ were discarded automatically because of their generally bad quality. Then CASSIS spectra were scaled to the predicted photospheres (Sect. 3.1) using the shortest wavelength parts of the spectra which are not contaminated by the emission from the disc. The scaling factor was less than 5% in all cases. Finally, those individual IRS modules that were not aligned with each other were stitched together using multiplicative correction factors estimated from the overlapping spectral regions.

3 ANALYSIS

3.1 Stellar properties

The spectral types of the selected stars range between B9 and F7. All of them are included in the *Hipparcos* catalogue (van Leeuwen 2007), their trigonometric distances lie between 28 and 90 pc. Our sample contains only one known multiple system. HD 16743 and HD 16699AB, the latter being a binary itself, form a wide multiple system with a minimum separation of $\sim 12700 \text{ au}$ ($\sim 216''$, Moór et al. 2011a;

Tokovinin & Lépine 2012). We searched for common-proper-motion (CPM) companions in the 0.1 pc vicinity for the other targets. Using the astrometric data from the UCAC4 catalogue (Zacharias et al. 2013) and criteria presented by Halbwachs (1983), we found no additional CPM candidates.

To characterize the disc excess emission, the contributions of the stellar photosphere and of the circumstellar dust grains to the measured flux must be separated. In order to predict the photospheric fluxes at relevant infrared and submillimetre wavelengths, and to estimate fundamental stellar properties, the photosphere was modelled by fitting an ATLAS9 atmosphere model (Castelli & Kurucz 2003) to the optical and near-IR observations. Photometric data were taken from the *Tycho 2* (Høg et al. 2000), *Hipparcos* (Perryman 1997), and Two Micron All Sky Survey catalogues (2MASS, Cutri et al. 2003). The data were further supplemented by Wide-field Infrared Survey Explorer (*WISE*) *W1* band (centred at 3.4 μm) photometry from the *WISE All-Sky Database* (Wright et al. 2010). *WISE* 4.6 μm measurements were not used because of the well known systematic overestimation effect of the fluxes of bright sources in this band (Sec. 6.3 of the Explanatory Supplement to the *WISE All-Sky Data Release Products*) In the case of HD 161868 and HD 195627, the 2MASS data were also discarded because of saturation. The metallicity data were collected from the literature. In those cases where more than one $[\text{Fe}/\text{H}]$ estimates were found, we used their average. If no metallicity data were available we adopted solar metallicity for the given target. The surface gravity values were determined via an iterative process. Initially we set $\log g = 4.5$ for all targets, performed the atmospheric model fitting, and estimated the luminosity and mass of the star as described below. Using the latter parameters and the derived effective temperatures, the $\log g$ values were re-interpolated in a grid with a stepsize of 0.25, and the fitting of the photometric data was repeated until $\log g$ converged at a grid point. The resulting values are listed in Table 2.

Our targets are located within 90 pc of the Sun, i.e. inside the relatively dust-free Local Bubble suggesting that their interstellar reddening might be negligible (e.g. Reis et al. 2011; Lallement et al. 2014). Apart from HD 95086 all of our stars have Strömgren *uvby* photometry and H_β indices in the catalogue compiled by Hauck & Mermilliod (1998). In order to further evaluate whether their reddening can be really neglected, we derived $E(B - V)$ values for the targets by applying the appropriate calibration processes (Crawford 1975, 1979; Olsen 1984). We found that none of our sources has interstellar extinction. In the case of HD 95086, the good agreement between the photometrically and spectroscopically estimated effective temperatures (Moór et al. 2013a) supports the negligible reddening. The effective temperature values yielded by the fitting as well as the derived stellar luminosities are presented in Table 2.

Among the 11 selected systems three can be assigned to young kinematic groups or associations. HD 9672 belongs to the ~ 40 Myr old Argus moving group (Zuckerman & Song 2012), and HD 21997 is part of the ~ 30 Myr old Columba (Moór et al. 2006; Torres et al. 2008) moving group. HD 95086 is a member of the Lower Centaurus Crux association (de Zeeuw et al. 1999; Moór et al. 2013a; Meshkat et al. 2013). In these cases we adopted the age

³ <http://irsa.ipac.caltech.edu/applications/Spitzer/SHA/>

⁴ The Cornell Atlas of Spitzer/IRS Sources (CASSIS) is a product of the Infrared Science Center at Cornell University, supported by NASA and JPL.

of the corresponding group for the star. Based only on its astrometric data taken from the *Hipparcos* catalogue, HD 182681 is a probable candidate member of the β Pic moving group, however, the highly uncertain radial velocity measurement of the star makes this classification doubtful (see Appendix). Thus, for HD 182681, as well as two other early type stars, HD 10939 and HD 17848, the age information were taken from Nielsen et al. (2013), who performed isochrone fitting for these objects. In order to indicate the possible younger age of HD 182681 we changed the lower limit of its age confidence interval quoted by Nielsen et al. (2013) to 19 Myr (taking into account the recent age estimate of β Pic moving group from Mamajek & Bell 2014). For age-dating HD 161868 and HD 195627, we used metallicity, effective temperature, and luminosity data from Table 2. We performed a Bayesian approach of age estimates following the method outlined by Nielsen et al. (2013) and using the isochrones compiled by Siess, Dufour, & Forestini (2000). For the remaining stars the age estimates were taken from the literature. The stellar masses were also taken from the literature or were estimated based on the appropriate Siess isochrones.

3.2 Basic image analysis

All of our targets appeared as very bright sources on PACS images in all bands. We searched the PACS maps for nearby ($<30''$) background sources. Figure 1 shows the PACS 100 μm images for those four targets where background sources were detected. At HD 17848 a background source is visible on the 100 μm and 160 μm images at $\sim 25''$ southwest from the target. On the maps of HD 50571 two additional sources can be identified at separations of $22''$ and $28''$. In the cases of HD 161868 and HD 195627 there are background objects to east with separations of $\sim 21''$ and $\sim 15''$, respectively. All of these background sources were found to be point-like, making it possible to subtract them after fitting appropriate point spread functions (PSFs) to them. We note that there is a bright source $33''$ away from HD 182681, but due to the large separation, it does not have a significant effect on our analysis.

As Figure 2 demonstrates, at 70 μm most of our sources look elongated and spatially extended compared with the PACS beam. Actually, in the case of HD 170773 our PACS 70 μm (and 100 μm) measurements resolve a broad ring of emission, i.e. even the inner edge of the dust ring was outlined. In order to evaluate whether the discs are indeed spatially extended we produced a first estimate of their position angles (PA, measured north through east), sizes, and inclinations (i , measured from face-on = 0°), which will be further refined in Sect. 4.3. Following a common procedure in the literature, we fitted 2D Gaussians to the images and compared the resulting parameters to those we derived for PSF observations. This approach is widely used in studies of *Herschel* resolved debris discs, therefore our results can be directly compared with similar results in the literature (e.g. Bonsor et al. 2013; Marshall et al. 2013; Matthews et al. 2014a).

PSFs for the different PACS bands were constructed using measurements of four photometric calibration stars (α Boo, α Tau, α Cet, β And) that do not exhibit infrared excesses. We collected all those observations of these targets

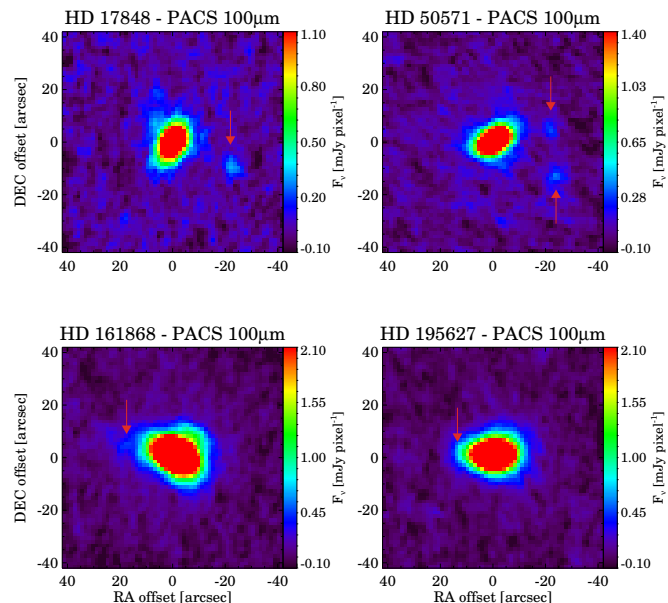


Figure 1. PACS 100 μm images of those objects where nearby background sources are present (Sect. 3.2). In the case of HD 195627 the background source cannot be separated from the disc by eye, however the distortion of the eastern part of the disc image indicates its presence. Red arrows show the positions of the background sources.

(14, 15 and 29 measurements at 70, 100, and 160 μm , respectively) that were obtained in the same observing mode and same period of the mission (between Operational Days 795 and 1035) as our targets, and processed them with HIPE using identical data reduction steps and parameters as described in Sect. 2.2.1. The PSFs then were rotated to match the roll angle of the telescope at the time of observing the specific source. This last step was needed because the shape of the *Herschel*/PACS PSFs were affected by the telescope’s tripod resulting in an asymmetric beam pattern that rotated with the satellite roll angle.

We found that apart from HD 16743 – which is spatially extended only at 100 μm , but consistent with a point-source at 160 μm – all of the targets are at least marginally extended in all bands. To estimate the discs’ sizes we made a quadratic deconvolution. We fitted 2D Gaussians to the appropriately rotated PSFs, then we derived the FWHM of the Gaussian along cuts parallel to the discs’ major and minor axes. By fitting all available PSFs we could compute the average of the corresponding FWHMs and estimate the uncertainties related to the possible beam variation (see also in Kennedy et al. 2012b). Then the disc angular sizes were derived as $\theta_{disc} = \sqrt{\theta_{image}^2 - \langle \theta_{PSF} \rangle^2}$, where θ_{image} is the derived FWHM of the image along the major or minor axis, $\langle \theta_{PSF} \rangle$ is the average size of the PSF in the appropriate direction, while θ_{disc} is the disc size along the major or minor axis. Assuming that the intrinsic structure of the disc is azimuthally symmetric, the inclination of the disc was also computed as the arc cosine of the axis ratio. Table 3 lists the disc parameters based on this quadratic deconvolution.

All of the targets are detected in the 250 and 350 μm

Table 2. Basic stellar properties. (1) SIMBAD compatible identifier of the star. (2) Spectral type. (3) Distance of the star based on trigonometric parallax taken from the *Hipparcos* catalogue (van Leeuwen 2007). (4) Derived effective temperature. (5) Surface gravity values fixed in the course of fitting stellar atmospheric models. (6) Metallicity data from the literature; if more than one observations are available the average of the $[\text{Fe}/\text{H}]$ is quoted. (7) References for metallicity data. 1 – Casagrande et al. (2011), 2 – Erspamer & North (2003), 3 – Gray et al. (2003), 4 – Gray et al. (2006), 5 – Montesinos et al. (2009), 6 – Soubiran et al. (2010), 7 – Wu et al. (2011). (8) Derived stellar luminosity. (9) Stellar mass. (10) References for stellar mass data. 1 – Meshkat et al. (2013), 2 – Moór et al. (2011b), 3 – Roberge et al. (2013), 4 – this work. (11) Estimated age of the star and its confidence interval. (12) References for age estimates. 1 – Meshkat et al. (2013), 2 – Moór et al. (2011a), 3 – Moór et al. (2011b), 4 – Nielsen et al. (2013), 5 – Rhee et al. (2007), 6 – this work, 7 – Zuckerman & Song (2012). (13) Group membership. (14) Measured projected rotational velocity. (15) References for rotational velocity. 1 – Abt, Levato, & Grosso (2002), 2 – Díaz et al. (2011), 3 – Głębcki & Gnaniński (2005), 4 – Moór et al. (2011a), 5 – Moór et al. (2013a), 6 – Nordström et al. (2004), 7 – Royer, Zorec, & Gómez (2007).

Target	Sp.T	Dist. [pc]	T_{eff} [K]	$\log g$	[Fe/H]	Ref.	L_* [L_{\odot}]	M_* [M_{\odot}]	Ref.	Age [Myr]	Ref.	Membership	$v \sin i$ [km s^{-1}]	Ref.
HD 9672	A1V	59.4	8900	4.25	0.10	5	16.4	2.00	3	40 [30,50]	7	Argus	196	7
HD 10939	A1V	62.0	9100	4.00	0.00	-	30.9	2.25	4	346 [305,379]	4	-	73	3
HD 16743	F0/F2III/IV	58.9	6950	4.25	-0.06	1	5.2	1.50	4	30 [10,50]	2	-	100	4
HD 17848	A2V	50.5	8450	4.25	0.00	-	15.7	1.93	4	372 [269,467]	4	-	144	2
HD 21997	A3IV/V	71.9	8300	4.25	0.00	-	11.2	1.85	2	30 [20,40]	3	Columba	70	7
HD 50571	F7III-IV	33.6	6550	4.25	0.00	1,4	3.2	1.30	4	300 [180,420]	2	-	60	6
HD 95086	A8III	90.4	7550	4.25	0.00	-	7.0	1.70	1	17 [13,21]	1	LCC	20	5
HD 161868	A0V	31.5	8950	4.00	-0.54	3,6,7	26.5	2.10	4	450 [312,532]	6	-	210	7
HD 170773	F5V	37.0	6650	4.25	-0.05	1,4	3.5	1.30	4	200 [-,-]	5	-	50	4
HD 182681	B8/B9V	69.9	9650	4.25	0.00	-	24.7	2.18	4	144 [19,208]	4	-	275	1
HD 195627	F1III	27.8	7300	4.00	-0.11	2,4	7.4	1.57	4	805 [462,1100]	6	-	114	3

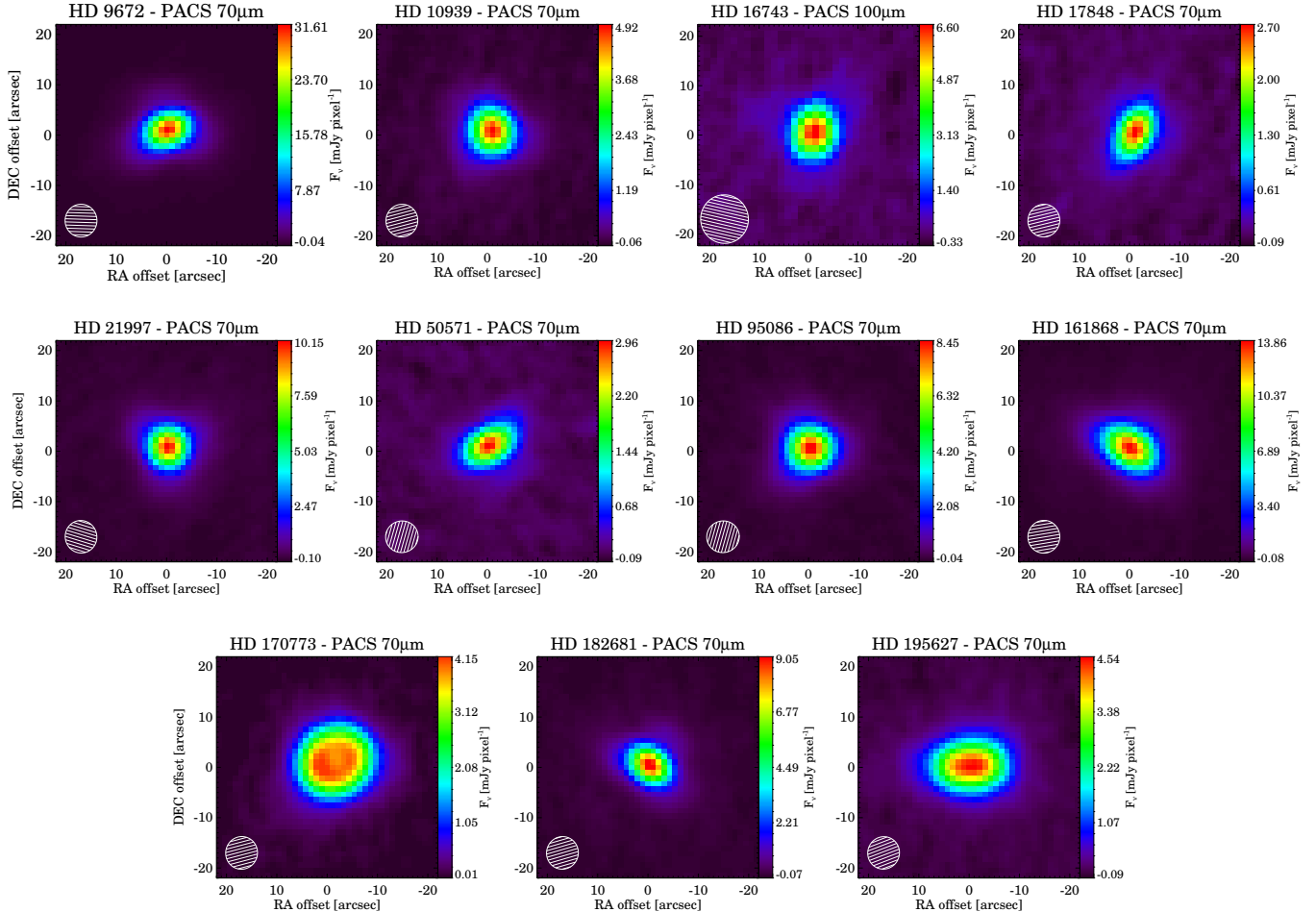


Figure 2. Resolved PACS images of our 11 targets at $70\mu\text{m}$ ($100\mu\text{m}$ for HD 16743 where no $70\mu\text{m}$ PACS image is available). The hatched ellipses in the lower left corners show the average FWHMs of the rotated PSFs.

Table 3. Results of 2D Gaussian disc fitting

Target	PACS band	Disc size ($\theta_{maj} \times \theta_{min}$)		i	PA
		[$''$]	[au]	[$^\circ$]	[$^\circ$]
HD 9672	70 μ m	6.5 \pm 0.2 \times 2.5 \pm 0.3	383 \pm 9 \times 147 \pm 16	67.4 \pm 2.7	109.0 \pm 3.9
	100 μ m	6.6 \pm 0.2 \times 2.6 \pm 0.3	392 \pm 9 \times 152 \pm 15	67.2 \pm 2.5	109.4 \pm 4.8
	160 μ m	7.0 \pm 0.9 \times 3.9 \pm 1.5	417 \pm 51 \times 229 \pm 90	56.7 \pm 15.5	93.4 \pm 13.9
HD 10939	70 μ m	6.1 \pm 0.3 \times 5.5 \pm 0.3	381 \pm 15 \times 340 \pm 16	26.8 \pm 7.2	25.1 \pm 15.8
	100 μ m	6.7 \pm 0.3 \times 5.9 \pm 0.3	417 \pm 17 \times 364 \pm 18	29.3 \pm 6.7	19.9 \pm 16.2
	160 μ m	7.7 \pm 0.9 \times 7.1 \pm 0.8	480 \pm 57 \times 439 \pm 52	23.8 \pm 21.8	70.4 \pm 24.0
HD 16743	100 μ m	6.3 \pm 0.5 \times 3.7 \pm 0.7	370 \pm 29 \times 216 \pm 38	54.2 \pm 8.0	165.4 \pm 17.4
HD 17848	70 μ m	7.7 \pm 0.4 \times 3.0 \pm 0.5	386 \pm 20 \times 149 \pm 26	67.3 \pm 4.4	153.8 \pm 7.3
	100 μ m	9.2 \pm 0.5 \times 3.9 \pm 0.5	465 \pm 23 \times 195 \pm 26	65.2 \pm 3.8	154.4 \pm 8.3
	160 μ m	10.6 \pm 1.5 \times 5.6 \pm 2.6	535 \pm 77 \times 284 \pm 131	58.0 \pm 17.3	147.8 \pm 17.6
HD 21997	70 μ m	4.9 \pm 0.3 \times 4.4 \pm 0.3	349 \pm 23 \times 313 \pm 23	26.1 \pm 11.9	24.7 \pm 27.5
	100 μ m	4.9 \pm 0.4 \times 4.3 \pm 0.4	350 \pm 26 \times 307 \pm 28	28.7 \pm 12.7	27.0 \pm 29.2
	160 μ m	6.1 \pm 1.2 \times 5.0 \pm 1.9	440 \pm 86 \times 360 \pm 137	35.1 \pm 35.0	56.4 \pm 37.8
HD 50571	70 μ m	7.8 \pm 0.5 \times 2.9 \pm 0.6	260 \pm 15 \times 96 \pm 20	68.2 \pm 5.0	121.2 \pm 8.5
	100 μ m	9.1 \pm 0.3 \times 3.3 \pm 0.7	306 \pm 9 \times 109 \pm 24	69.0 \pm 5.0	120.7 \pm 7.3
	160 μ m	10.6 \pm 1.1 \times 4.8 \pm 2.2	357 \pm 36 \times 161 \pm 73	63.1 \pm 13.6	133.3 \pm 13.0
HD 95086	70 μ m	6.0 \pm 0.2 \times 5.5 \pm 0.2	543 \pm 15 \times 499 \pm 15	23.3 \pm 5.6	100.6 \pm 15.6
	100 μ m	6.4 \pm 0.2 \times 5.6 \pm 0.2	575 \pm 16 \times 508 \pm 17	27.9 \pm 4.9	114.0 \pm 15.9
	160 μ m	7.2 \pm 0.8 \times 6.8 \pm 0.8	655 \pm 73 \times 614 \pm 75	20.3 \pm 25.9	139.1 \pm 15.5
HD 161868	70 μ m	8.5 \pm 0.1 \times 4.7 \pm 0.1	269 \pm 1 \times 148 \pm 1	56.6 \pm 0.6	59.2 \pm 1.0
	100 μ m	9.7 \pm 0.1 \times 5.0 \pm 0.2	304 \pm 2 \times 158 \pm 5	58.7 \pm 1.3	61.1 \pm 2.6
	160 μ m	10.9 \pm 0.7 \times 5.4 \pm 0.8	344 \pm 21 \times 171 \pm 25	60.1 \pm 5.3	66.1 \pm 6.5
HD 170773	70 μ m	11.8 \pm 1.1 \times 10.1 \pm 0.8	435 \pm 39 \times 372 \pm 29	31.2 \pm 11.4	115.3 \pm 24.0
	100 μ m	11.8 \pm 0.4 \times 10.1 \pm 0.4	435 \pm 14 \times 373 \pm 13	30.9 \pm 4.6	116.9 \pm 18.7
	160 μ m	11.4 \pm 1.2 \times 9.8 \pm 1.1	422 \pm 46 \times 362 \pm 41	31.0 \pm 15.2	99.5 \pm 21.7
HD 182681	70 μ m	5.8 \pm 0.1 \times 2.2 \pm 0.3	403 \pm 8 \times 156 \pm 20	67.2 \pm 3.2	56.0 \pm 3.9
	100 μ m	5.7 \pm 0.2 \times 2.1 \pm 0.4	401 \pm 14 \times 144 \pm 25	68.9 \pm 4.0	55.7 \pm 7.3
	160 μ m	6.6 \pm 1.0 \times 2.6 \pm 2.3	459 \pm 69 \times 184 \pm 161	66.3 \pm 22.3	63.5 \pm 19.3
HD 195627	70 μ m	11.6 \pm 0.2 \times 6.9 \pm 0.3	323 \pm 5 \times 190 \pm 8	53.9 \pm 1.9	92.4 \pm 3.7
	100 μ m	12.9 \pm 0.3 \times 7.3 \pm 0.2	358 \pm 7 \times 202 \pm 6	55.7 \pm 1.5	91.0 \pm 4.3
	160 μ m	15.6 \pm 0.5 \times 7.7 \pm 1.0	432 \pm 15 \times 212 \pm 28	60.5 \pm 4.4	89.0 \pm 5.2

SPIRE maps. HD 9672, HD 161868, HD 170773 and HD 195627 are visible at 500 μ m as well. Four of our targets – HD 10939, HD 16743, HD 17848, and HD 50571 – are detected at submillimetre wavelengths for the first time. HD 170773 and HD 195627 are found to be marginally extended at 250 μ m and 350 μ m when compared to the corresponding SPIRE beam (taken from the SPIRE calibration context). In the latter case the emission is extended with the same position angle of $\sim 90^\circ$ as in the PACS images. We note, however, that the very nearby background source is also located along the same PA. Considering the low inclination of HD 170773, the object is not particularly elongated in the SPIRE images, and the PA can only be determined with a large uncertainty. HD 161868 lies on the top of background emission originated from an extended ridge that is especially bright at 500 μ m thus, we do not attempt to derive geometrical parameters from the SPIRE images for this source.

3.3 PACS and SPIRE photometry

The source flux determination was performed on the final *Herschel* PACS mosaics after the nearest background sources were removed from the affected images (Sect. 3.2). We used aperture photometry by placing the apertures at the centroid position. We found that the offsets between

the sources' optical positions (corrected for the proper motion using the epochs of PACS observations) and the derived centroids in the PACS images are $\leq 2''/4$ for most of our targets, i.e. within the 1σ pointing accuracy of *Herschel*. Even the largest offset of $3''/2$, measured for HD 10939 is well within the 2σ pointing uncertainty of the telescope. The aperture radius was chosen to cover the resolved disc emission: $24''$ for HD 170773 and HD 195627, and $20''$ for the other sources. We used the same aperture size at all wavelengths. The background was always computed in a sky annulus between $50''$ and $60''$. To remove the possible contamination of any remaining background objects, we used an iterative sigma-clipping method with a 3σ clipping threshold in the sky annulus. In order to estimate the sky noise in each PACS band, we distributed sixteen apertures, with the same size as the source aperture, randomly along the background annulus. We performed aperture photometry without background subtraction in each aperture and computed the sky noise as the standard deviation of derived background flux values. Finally we applied aperture correction to account for the flux outside the aperture using correction factors taken from the appropriate calibration file. According to our tests, in the case of the selected aperture configurations the nominal correction factors for point sources can be safely applied. The total uncertainty of the photometry was derived as the quadratic sum of the measurement errors and the ab-

solute calibration uncertainty of 7% (Balog et al. 2013). We note that in most cases, especially at 70 and 100 μm , the uncertainty of the absolute calibration dominates the error budget.

Background sources discovered in PACS images close to some targets might also be present in SPIRE maps. However, because of the coarser spatial resolution, in most cases they cannot be clearly deblended from our main targets. In order to minimize the possible contamination of these sources (and possible additional ones) and the extended background emission in the case of HD 161868, we used PSF fitting in the flux determination. Apart from HD 170773 and HD 195627, which were found to be marginally extended at 250 μm and 350 μm , we used the SPIRE beam profiles taken from the calibration context in the course of flux extraction. For HD 170773 and HD 195627 at 250 μm and 350 μm the original SPIRE beam was convolved with a 2D Gaussian whose parameters (FWHM of the major and minor axes, position angle) were taken from the Gaussian fitting performed at 100 μm (Sect. 3.2, Table 3). The offsets between the stellar positions corrected for the proper motion and the sources' centroids are generally smaller than $3''$, corresponding to 1.3σ pointing uncertainty of *Herschel*. The only exception is HD 195627, where the flux peak is shifted by 5 – $6''$ east of the nominal stellar position raising a complicated issue since the nearby source is also located to the east, and the disc is elongated in the east-west direction too. In this case we placed the centre of the aperture at the nominal stellar position, but some contamination from the background source cannot be excluded. The final uncertainties were derived as the quadratic sum of the measurement errors and the overall calibration uncertainty of 5.5% for the SPIRE photometer (Bendo et al. 2013).

The derived PACS and SPIRE flux densities of the targets are listed in Table 4. We note that PACS and SPIRE photometry of HD 21997 and HD 95086 were taken from Moór et al. (2013b) and Moór et al. (2013a), respectively.

3.4 MIPS photometry

When performing photometry in MIPS 70 μm maps we utilized the spatial information from the higher resolution PACS 70 μm images. As a first step, a PSF profile valid for sources with blackbody temperatures of 60 K was constructed using the method described by Gordon et al. (2007). The compiled PSF was convolved with a two-dimensional elliptical Gaussian constructed for each source by using the parameters derived from the Gaussian fitting in the PACS 70 μm image. These spatially extended profiles were used to determine the flux density of the targets via PSF fitting. The final photometric uncertainty was computed by quadratically adding the calibration uncertainty of 7% (Gordon et al. 2007) and the measurement error. The MIPS 70 μm band photometry (with an effective filter wavelength of 71.42 μm) shows a good agreement with the PACS 70 μm photometry. If we take into account the typical color correction factors of 0.9 and 0.98 for MIPS and PACS photometry, respectively, the flux densities obtained with the two instruments at different epochs are consistent with each other within their 1σ uncertainty.

From *Herschel* we know that the discs are spatially extended at 160 μm as well. However, the MIPS 160 μm beam

is significantly larger than the size of the discs. Therefore the sources can be considered as point-like, and the 160 μm photometry was simply taken from Moór et al. (2011a) when available. Photometry in MIPS 24 μm filter were also taken from the literature. MIPS photometric data for our sources are also listed in Table 4.

4 RESULTS

4.1 Disc properties derived from SEDs

We compiled the SED of each object by combining the optical and near-IR data points (see Sect. 3.1) with the new PACS, SPIRE and MIPS flux densities and photometry obtained by different infrared space missions and ground-based submillimetre observations. IRAS photometry with moderate quality (quality index of 2) was re-evaluated by utilizing the SCANPI tool⁵. In most cases the results were consistent with the values quoted in the IRAS catalogues, except for HD 182681 where at 60 μm we adopted the photometry derived from SCANPI (0.549 ± 0.100 Jy). References for the utilized catalogues and literature data are summarized in Table 4. *Spitzer* IRS spectra of the targets are found to be featureless. For the subsequent SED modelling process the IRS spectra were resampled into the following 11 adjacent wavelength bins: 10–12, 12–14, 14–16, 16–18, 18–20, 20–23, 23–26, 26–29, 29–32, and 32–35 μm . In the computation of uncertainties of the derived flux densities in a given bin, we adopted 5% absolute calibration uncertainty for IRS added in quadrature. The SEDs for HD 21997 and HD 95086 were adopted from Moór et al. (2013b) and Moór et al. (2013a), respectively. The constructed SEDs are plotted in Figure 3.

The infrared excess emission of debris discs is attributed to optically thin thermal emission of second generation circumstellar dust grains. In most cases the measured excess emission can be well fitted by a single temperature modified blackbody or a combination of two different temperature components that are thought to represent narrow, spatially separated warm and cold rings in which the bulk of the emitting dust grains is confined. This simple model/assumption can provide estimates of some basic disc properties, e.g. the characteristic dust temperature(s) and the fractional luminosity (the ratio of the integrated luminosity of the dust emission to the integrated luminosity of the host star).

In the course of modelling we fitted the excess emission that was derived as a difference between the measured flux densities and the predicted photospheric fluxes. The average accuracy of the predicted photospheric fluxes is estimated to be around 3%. The final errors in the excess flux densities were computed as a quadratic sum of uncertainties of the measured and the predicted photospheric fluxes. In the case of HD 161868 the SPIRE measurement at 500 μm deviated significantly from the trend delineated by other submillimetre observations (see Fig. 3). This source coincides with bright background emission at this wavelength (Sect. 3.2) and notwithstanding the applied PSF photometry the measured flux density may be affected by background contamination. Therefore this data point was ignored in the SED

⁵ <http://scanpiops.ipac.caltech.edu:9000>

Table 4. Photometric data used in SED compilation. (1) SIMBAD compatible identifier of the star. (2-10) Measured flux densities in PACS, SPIRE, and MIPS bands. The quoted fluxes are in mJy and are not colour-corrected. For HD 21997 and HD 95086 these photometric data were taken from Moór et al. (2013b) and Moór et al. (2013a), respectively. (11) References for MIPS photometry: 1 – Ballering et al. (2013), 2 – Moór et al. (2011b), 3 – Roberge et al. (2013), 4 – this work. (12) References for additional infrared and ground-based submillimetre photometric data: 1 – IRAS PSC, 2 – IRAS FSC, 3 – Ishihara et al. (AKARI IRC 2010), 4 – Moór et al. (2011b), 5 – Nilsson et al. (2010), 6 – Panić et al. (2013), 7 – Su et al. (2008), 8 – Williams & Andrews (2006), 9 – Wright et al. (WISE 2010), 10 – Yamamura et al. (AKARI FIS 2010)

Target	PACS			SPIRE			MIPS			Refs.	Additional photometry
	70 μ m	100 μ m	160 μ m	250 μ m	350 μ m	500 μ m	23.675 μ m	71.42 μ m	155.9 μ m		
HD 9672	2163 \pm 151	1919 \pm 134	1066 \pm 75	363 \pm 20	166 \pm 11	76 \pm 8	259 \pm 10	1749 \pm 123	-	3,4	2,3,9,10
HD 10939	396 \pm 28	403 \pm 28	277 \pm 20	94 \pm 7	43 \pm 6	3 \pm 6	108 \pm 4	379 \pm 27	-	1,4	2,3,9
HD 16743	-	369 \pm 27	226 \pm 32	82 \pm 6	38 \pm 6	8 \pm 8	50 \pm 2	388 \pm 26	174 \pm 24	2,4	2,3,9
HD 17848	213 \pm 17	210 \pm 18	138 \pm 11	50 \pm 5	28 \pm 6	6 \pm 10	86 \pm 3	204 \pm 17	-	1,4	2,3,9
HD 21997	697 \pm 49	665 \pm 47	410 \pm 30	151 \pm 11	66 \pm 9	33 \pm 9	55 \pm 2	663 \pm 46	-	1,4	2,3,8,9
HD 50571	223 \pm 17	262 \pm 19	188 \pm 16	71 \pm 7	46 \pm 6	13 \pm 7	70 \pm 2	235 \pm 17	214 \pm 36	2,4	2,3,9
HD 95086	690 \pm 48	675 \pm 47	462 \pm 32	213 \pm 12	120 \pm 8	63 \pm 10	45 \pm 2	655 \pm 44	-	1,4	1,3,9
HD 161868	1222 \pm 85	1051 \pm 73	587 \pm 44	177 \pm 12	98 \pm 10	56 \pm 11	434 \pm 18	1118 \pm 78	-	1,4	1,3,6,7,9
HD 170773	806 \pm 56	1109 \pm 78	875 \pm 61	379 \pm 21	167 \pm 11	73 \pm 7	65 \pm 2	785 \pm 55	692 \pm 83	2,4	1,3,4,5,9
HD 182681	607 \pm 42	463 \pm 33	243 \pm 18	84 \pm 7	30 \pm 5	8 \pm 7	-	-	-	1,4	2,3,6,9
HD 195627	629 \pm 44	607 \pm 43	405 \pm 29	145 \pm 14	70 \pm 7	34 \pm 7	204 \pm 8	644 \pm 45	-	1,4	1,3,5,9,10

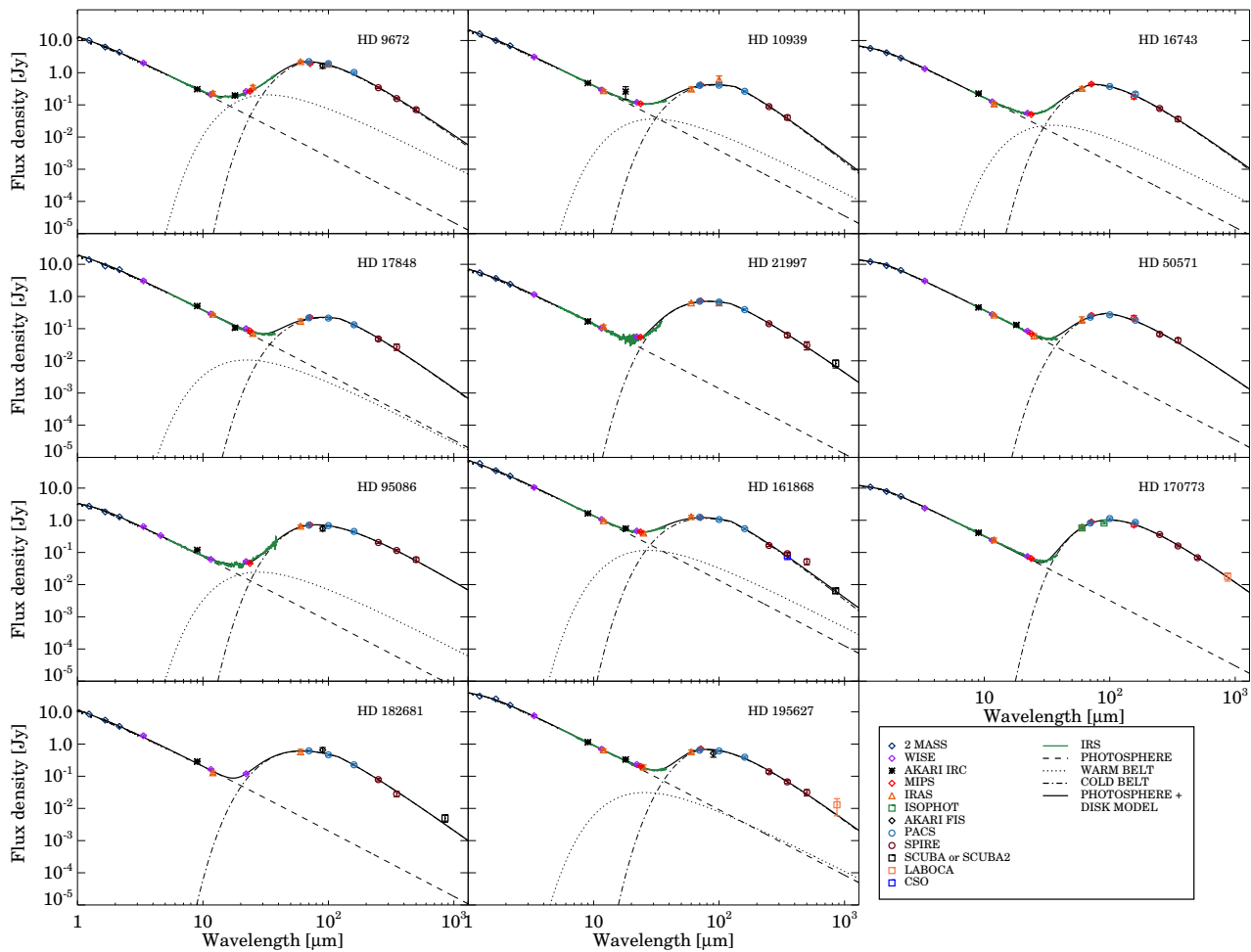


Figure 3. SEDs of the studied systems. Stellar photospheres and the best fit models (Sect. 4.1) are also displayed.

fitting. The IRAS FSC catalogue includes a moderate quality 100 μm photometry for HD 16743. This measurement was also omitted, because the quoted flux density is inconsistent with the much better quality PACS photometry.

The excess SEDs were fitted by single temperature and two-temperature models. For the single temperature approach we used a modified blackbody where the emissivity is equal to 1 at $\lambda \leq \lambda_0$ and follows $(\lambda/\lambda_0)^{-\beta}$ for longer wavelengths. Here we fitted four parameters, A_c a scaling factor that is proportional to the solid angle of the emitting region, $T_{\text{bb},c}$, λ_0 , and β . In the two-temperature model, we added a warmer simple blackbody component (characterized by two parameters, A_w and $T_{\text{bb},w}$) to the one defined above. The best-fitting model was found by applying a Levenberg-Marquardt algorithm (Markwardt 2009). An iterative way was used to compute and apply colour corrections for the photometric data during the fitting process (see e.g. Moór et al. 2006).

In order to decide whether the single-temperature or the two-temperature model is better for a given source, we applied a variant of the Akaike Information Criterion, the so-called corrected AIC_c (Burnham & Anderson 2002). By penalizing the usage of unnecessary additional model parameters, this method provides a way to compare the relative quality of different models. The corrected AIC_c was derived as:

$$AIC_c = \chi^2 + 2k + \frac{2k(k+1)}{n-k-1} \quad (1)$$

where n is the number of observations, and k is the number of parameters in the model. Better model quality gives a lower AIC_c . Based on this test, we found the single-component model to be better only in four cases (HD 21997, HD 50571, HD 170773, HD 182681). The best-fit models for each of our targets are plotted in Figure 3.

The fractional luminosity of the discs was computed as $f_{\text{dust}} = L_{\text{dust}}/L_{\text{bol}}$. The integrated dust emission was derived using the fitted models. Based on the derived characteristic temperatures and the stellar luminosities (Table 2), dust belt radii valid for large blackbody grains, were also derived following Backman & Paresce (1993):

$$\frac{R_{\text{bb}}}{\text{au}} = \left(\frac{L_{\text{star}}}{L_{\odot}} \right)^{0.5} \left(\frac{278 \text{ K}}{T_{\text{bb}}} \right)^2. \quad (2)$$

In the case of two-temperature models we assumed that the warm and cold components correspond to two spatially distinct dust belts and determined radii for the cold and warm component separately. T_{bb} is set equal to the temperature values ($T_{\text{bb},w}$ and $T_{\text{bb},c}$, for the warm and cold components, respectively) found in our fitting process.

The obtained fundamental disc properties are listed in Table 5.

All of our targets were successfully detected at submillimetre wavelength that allowed us to estimate the dust mass in the system. We followed the standard approach assuming optically thin emission characterized by a single temperature (in our case, the temperature of the cold component):

$$M_d = \frac{F_{\nu, \text{excess}} d^2}{B_{\nu}(T_{\text{bb},c}) \kappa_{\nu}}, \quad (3)$$

where $F_{\nu, \text{excess}}$ is the measured excess at the longest wavelength where submillimetre data is available (except in the

case of HD 195627 where we used the 500 micron SPIRE data point instead of the 870 micron LABOCA measurement that has low signal-to-noise ratio), d is the distance to the source, $\kappa_{\nu} = \kappa_0 (\frac{\nu}{\nu_0})^{\beta}$ is the mass absorption coefficient, and B_{ν} is the Planck function. We adopted $\kappa_0 = 2 \text{ cm}^2 \text{ g}^{-1}$ at $\nu_0 = 345 \text{ GHz}$ (e.g. Nilsson et al. 2010), the β and $T_{\text{bb},c}$ values were taken from Table 5. The derived dust masses and their uncertainties are also listed in Table 5.

4.2 Geometrical disc model

In order to precisely derive geometrical parameters for the discs around our targets, we fitted the PACS images using a simple, non-physical disc model grid. In our first approach, we assumed that the emitting dust is located in a narrow ring around the central star. Such a geometry could be expected from our SED modeling, where we found that the long-wavelength excess could be fitted with a single temperature modified blackbody, the cold component in Table 5. Our simple model has three free parameters, the average disc radius (R_{avg}), the position angle (PA) and the inclination (i) of the disc. This disc is assumed to be $0.1 R_{\text{avg}}$ wide, i.e. it extends from $0.95 R_{\text{avg}}$ to $1.05 R_{\text{avg}}$ in radial direction. We calculated 6048 models in a regular grid. We used 18 different position angles centred on the value determined from the 2D Gaussian fitting (Sect. 3.2), with a step between 0.5 and 10° (larger step for longer wavelengths and for more face-on discs, and smaller step for shorter wavelengths and more edge-on discs). We took 21 different inclinations from 0 to 90° , using a regular grid for $\cos i$. For the average disc radius, we used 16 different values, centred on those obtained from the Gaussian fitting, and a step between 2 and 8 au (smaller for smaller discs and shorter wavelengths, larger for larger discs and longer wavelengths). The surface brightness of the disc was assumed to be homogeneous. In each model, we included a central point source as well, meant to represent the emission from the stellar photosphere and from the warm inner dust ring where exist. The flux ratio of the central point source to the disc in our model was adjusted to match the respective flux ratio of each target from the SED modeling. These model images were then convolved with a PSF appropriately rotated to match the PSF angle of each observation (for the PSF we used the observation of α Boo with OBS ID 1342247705 at $70 \mu\text{m}$ and with OBS ID 1342223348 at 100 and $160 \mu\text{m}$). The convolved model images were then down-sampled and shifted to match the pixel size and astrometry of the actual observations.

In order to select the best-fitting model from our grid, we used Bayesian analysis. We added in quadrature pixel values of the residual image (the difference of the model image and the observed image) in an aperture centred on the source, did the same in the error image, and took the ratio of the two numbers as χ^2 . The Bayesian probability assigned to a certain model is $\exp(-\chi^2/2a)$, where a is the area of the aperture. We then marginalized the Bayesian probabilities and obtained 1D probability distributions as a function of the three free parameters in the model. We fitted the distributions with Gaussians to determine the optimal value of R_{avg} , PA , and i . In cases where the probability distribution for the position angle was too wide, we fitted it with a von Mises distribution, the circular equivalent of

Table 5. Results of modified blackbody fitting.

Target	Warm component				Cold component				
	$T_{bb,w}$ [K]	$f_{d,w}$ [10^{-5}]	$R_{bb,w}$ [au]	$T_{bb,c}$ [K]	λ_0 [μm]	β	$f_{d,c}$ [10^{-5}]	$R_{bb,c}$ [au]	M_d [M_{\oplus}]
HD 9672	155±13	20.0±2.2	12.9±2.2	56±4	62±31	0.83±0.11	90.2±3.3	99±17	0.267±0.041
HD 10939	167±41	2.2±0.5	15.4±7.7	54±2	135±42	1.18±0.24	9.9±1.0	143±13	0.051±0.014
HD 16743	146±35	6.7±2.4	8.2±4.0	50±3	71±22	0.95±0.21	44.7±3.1	70±10	0.058±0.015
HD 17848	228±38	1.2±0.3	5.9±2.0	55±5	123±24	0.92±0.35	6.5±0.5	101±21	0.028±0.011
HD 21997	-	-	-	61±1	123±31	0.82±0.23	5.7±0.1	67±4	0.163±0.047
HD 50571	-	-	-	46±2	93±35	0.81±0.21	1.3±0.1	64±6	0.029±0.007
HD 95086	184±31	15.4±1.8	6.1±2.1	54±2	60±30	0.37±0.09	150.1±5.5	67±6	0.688±0.130
HD 161868	186±51	2.4±0.6	11.5±6.3	66±3	125±44	1.10±0.13	10.3±0.9	89±9	0.022±0.004
HD 170773	-	-	-	37±2	35±30	0.92±0.11	5.1±0.1	100±11	0.178±0.053
HD 182681	-	-	-	82±1	120±28	0.83±0.18	2.8±0.1	56±2	0.067±0.018
HD 195627	199±81	1.9±0.8	5.3±4.3	45±2	60±41	0.97±0.15	11.5±0.8	102±13	0.032±0.008

the Gaussian. With the optimal parameters, we calculated a model image and residuals. The residual images showed that our optimal models do not fit the observed images very well. For all targets, bright residuals at the stellar position and at large radial distances, and dark residuals in-between could be seen. This effect is strongest at the best resolution 70 μm images, but still noticeable for some sources at 100 μm . At 160 μm , the residuals were in all cases below 3σ .

The structure of the residual images at 70 μm strongly suggests that the adopted model geometry – a narrow ring – is not appropriate for our targets. For this reason, as a next step, we used an annulus, i.e. a disc with an inner hole. It was characterized by five free parameters: the average radius (R_{avg}), the position angle (PA), the inclination (i), the power law exponent of the brightness profile (p), and the thickness of the disc (t), defined so that the inner radius is at $R_{\text{avg}}(1 - t/2)$, while the outer radius is at $R_{\text{avg}}(1 + t/2)$. We calculated a grid of 848 160 models, with 18 different PA , 31 different i , 20 different R_{avg} , 19 different t , and 4 different p values. The disc thickness t was varied from 0.1 to 1.9 with a regular step of 0.1, while the range and step of the other parameters were the same as above. We found that the p values are not well constrained from the images. Moreover, they are degenerated with the inner and outer disc radii: steeper disc radial profiles are accompanied with tendentially larger inner/outer radii. For the further analyses we adopted $p = 0$ for all sources except HD 9672 and HD 161868, where a steeper profile with $p = -1$ provided significantly better fits. Bayesian analysis, fitting of the optimal parameters (listed in Table 6), calculating the best-fit model image and residuals (shown in Figure 4 for observations at 100 μm) were done as described above.

We note that the disc position angles and inclinations derived in the narrow and broad geometrical models were fully consistent with each other, and the PA values were also in good agreement with the ones obtained from 2D Gaussian fittings. As for disc inclinations, the 2D Gaussian and the geometrical models gave similar results below $i = 60^\circ$, while in more edge-on systems the Gaussian model provided somewhat lower inclination. Apart from the case of HD 170773, the inner edge of the outer dust belt has not been resolved, and its relative uncertainty is usually comparable to the derived R_{in} values. The average and the outer radii, however are better determined, and for any given object the deduced 70, 100, and 160 μm outer radii agree within their uncertainties.

Table 6. Disc properties derived from the geometrical model.

Target	PACS band (μm)	R_{avg} (au)	R_{in} (au)	R_{out} (au)	i ($^\circ$)	PA ($^\circ$)
HD 9672	70.0	253.0±13.5	46±28	459±28	84.1±5.9	109.4±1.6
	100.0	264.4±21.0	52±41	476±41	79.7±6.0	109.2±1.8
	160.0	227.1±24.5	83±58	371±58	77.7±10.8	110.5±4.5
	WMEAN	251.2±10.3	52±21	452±21	81.4±3.9	109.4±1.2
HD 10939	70.0	153.8±16.5	47±31	260±31	35.8±10.0	16.5±14.7
	100.0	171.3±20.0	69±36	273±36	32.5±10.0	20.1±13.6
	160.0	185.3±33.9	115±78	290±78	23.1±34.0	20.8±51.9
	WMEAN	163.9±11.9	61±23	267±23	34.1±7.1	18.5±9.8
HD 16743	100.0	156.6±19.7	72±39	240±39	58.5±8.3	165.0±6.7
HD 17848	70.0	156.1±17.3	45±42	266±42	77.1±9.7	154.6±5.0
	100.0	182.6±21.6	63±52	301±52	69.3±9.6	159.3±6.4
	160.0	215.8±47.5	47±173	384±173	75.6±22.6	154.6±14.6
	WMEAN	170.1±13.0	52±32	283±32	73.4±6.5	156.3±3.8
HD 21997	70.0	133.6±14.8	42±28	224±28	28.6±15.7	3.1±19.9
	100.0	139.3±17.2	72±35	206±35	19.0±15.3	4.7±36.8
	160.0	168.6±30.7	91±75	245±75	25.8±25.4	30.8±43.7
	WMEAN	139.9±10.5	57±21	219±21	24.0±10.1	7.2±16.2
HD 50571	70.0	99.9±11.5	30±29	168±29	80.7±10.4	119.2±5.2
	100.0	123.4±13.7	46±29	200±29	76.1±8.7	120.8±4.3
	160.0	135.1±26.6	39±85	230±85	78.1±18.3	120.0±11.1
	WMEAN	112.1±8.4	38±20	187±20	78.0±6.3	120.1±3.2
HD 95086	70.0	205.5±17.4	44±33	366±33	29.1±9.6	91.4±12.6
	100.0	217.8±25.1	72±45	363±45	24.2±13.0	106.0±17.6
	160.0	268.3±36.2	170±79	366±79	17.5±18.2	129.2±41.0
	WMEAN	217.4±13.3	66±25	365±25	25.9±7.1	98.3±9.9
HD 161868	70.0	156.2±7.6	50±14	261±14	64.9±1.9	57.8±1.8
	100.0	177.8±10.0	54±19	300±19	63.7±2.0	60.6±1.6
	160.0	164.4±12.5	35±26	292±26	64.3±5.3	60.8±4.2
	WMEAN	164.2±5.4	49±10	278±10	64.3±1.3	59.5±1.2
HD 170773	70.0	171.5±3.7	74±8	268±8	30.7±3.0	118.1±5.4
	100.0	175.9±4.6	89±10	262±10	31.7±2.3	117.4±4.3
	160.0	176.7±14.7	93±27	259±27	31.0±5.3	123.1±9.4
	WMEAN	173.4±2.8	81±6	265±6	31.3±1.7	118.3±3.2
HD 182681	70.0	154.3±15.8	44±31	263±31	79.5±4.8	54.1±3.3
	100.0	164.5±21.4	73±44	255±44	80.9±9.6	56.2±5.3
	160.0	175.7±54.1	59±198	410±198	84.2±21.5	59.0±17.8
	WMEAN	158.8±12.4	52±25	263±25	79.9±4.2	54.8±2.8
HD 195627	70.0	113.7±6.1	15±12	212±12	54.4±1.9	93.1±2.2
	100.0	124.7±8.4	25±17	224±17	55.9±2.2	92.1±2.7
	160.0	151.4±15.5	65±35	237±35	59.0±4.9	89.1±5.4
	WMEAN	120.6±4.7	22±9	217±9	55.4±1.4	92.4±1.6

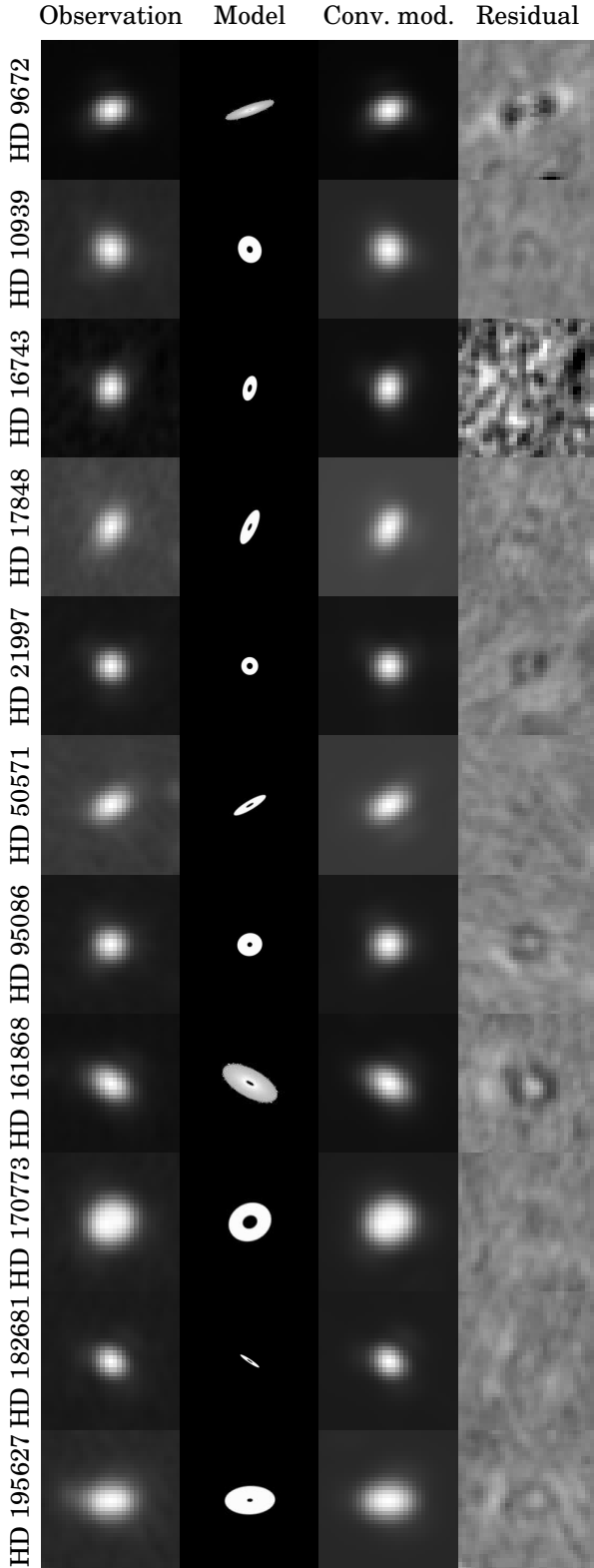


Figure 4. Measured and model images, as well as the residuals for the $100\ \mu\text{m}$ band observations of our 11 targets.

For each object we calculated the weighted averages of the different disc parameters obtained in different PACS bands (Table 6).

4.3 Comparison of our results to previous resolved data

Five of our targets have been successfully resolved by other instruments. The disc around HD 9672 has been spatially resolved in mid-IR thermal emission using the Keck telescope by Wahhaj, Koerner, & Sargent (2007). They derived a position angle of $125\pm 10^\circ$ and an inclination of $60\pm 15^\circ$ for the disc, both parameters are consistent with our results. Wahhaj, Koerner, & Sargent (2007) argued that the observed mid-IR emission dominantly comes from an inner disc component. Roberge et al. (2013) found this disc to be significantly extended at a position angle of $\sim 114^\circ$ based on a previous $70\ \mu\text{m}$ *Herschel* image (we used a later deeper observation in our analysis) of the source. They derived a disc radius of 200 AU, and constrained its inclination to be $\geq 44^\circ$.

In the case of HD 21997, our ALMA observation (Moór et al. 2013b) clearly resolved a broad ring of emission between 55 and 150 au, with a position angle of $21^\circ.5\pm 3^\circ.5$ and an inclination of $32^\circ.9\pm 2^\circ.6$. Apart from the outer radius all of these parameters match well the PACS-based values within the uncertainties. The outer edge of the disc is somewhat smaller in the ALMA image, indicating that the large grains may have a more confined distribution than the smaller grains emitting in the PACS bands. Moreover, ALMA is an interferometer, and may have filtered out some disc emission at the largest spatial scales (see more details in Moór et al. 2013b).

The disc around HD 161868 was resolved both at 24 and $70\ \mu\text{m}$ with the *Spitzer Space Telescope* (Su et al. 2008). They derived a disc position angle and inclination of $55\pm 2^\circ$ and $50\pm 5^\circ$, respectively, which are broadly consistent with our values ($PA=59^\circ.5\pm 1^\circ.2$ and $i=64^\circ.3\pm 1^\circ.3$). With a radius of 520 au at $70\ \mu\text{m}$, the disc was found to be somewhat more extended than in our analysis based on the PACS images, although this comparison is hampered by the coarser spatial resolution of *Spitzer*.

Analyzing the *Spitzer* MIPS $70\ \mu\text{m}$ images of HD 50571 and HD 170773, Moór et al. (2011a) revealed marginally extended emission at these sources. The disc around HD 50571 was found to be extended only in one direction along a position angle of 91° with a characteristic radius of ~ 160 au, which deviate from the PA of 120° and R_{avg} of 112 au derived from our PACS images. This discrepancy may partly be related to those nearby background sources, which are blended with the disc on *Spitzer* images. The characteristic radius of 180 au and position angle of 110° derived for HD 170773 are in good agreement with our new results based on PACS data (see Table 6).

5 DISCUSSION

5.1 General points concerning the disc parameters

Systems with warm inner belts. All of our targets harbour cold, extended outer dust component. In seven cases

(64%) our SED analysis implies the existence of a warmer component as well (Sect. 4.1). This fraction is consistent with the results of Chen et al. (2014) who found that in a large sample of 499 debris discs exhibiting *Spitzer*/IRS excess, two-temperature models provided better fit in 66% of the systems. That the SED analysis indicates two components with different temperatures does not necessarily mean that the system harbours a spatially distinct inner dust belt as well. Kennedy & Wyatt (2014) pointed out the possibility that the emission from a single narrow dust belt including grains with different sizes and thereby different temperatures can reproduce a two-component SED. However, this model may not be feasible for our seven discs: by placing them in Figures 13–15 of Kennedy & Wyatt (2014) these systems are clearly out of the parameter space covered by the single narrow disc models, although the fact that our discs are radially extended might slightly change this conclusion.

Supposing that in most of our cases the warm and cold components are associated with spatially distinct dust belts, what could be the origin of the warm dust? In our case the temperature of the warm dust component ranges between 145 and 230 K, where sublimation is an active process in comets ($T > 110$ K, Wyatt 2008). Therefore, the production of warm grains is not limited to collisions in the inner dust belt, but sublimation of icy bodies, originated from the outer planetesimal belt and entering the inner part of the system, can also contribute. We know a smaller number of warm debris discs where the dust production may be due to a recent transient event, e.g. collisions between large planetesimals (Wyatt 2008; Telesco et al. 2005; Stark et al. 2014). In order to evaluate whether the warm components discovered around our targets might be related to similar transient events, we utilized the analytical steady state model of Wyatt et al. (2007). Their model describes the collisional evolution of a planetesimal belt, and argues that at any given age there is a maximum dust fractional luminosity (f_{max}), since initially more massive discs consume their mass faster. Wyatt et al. (2007) proposed that dust belts with fractional luminosity of $\gg 100 \times f_{max}$ can be considered as a result of a transient event that increases the dust production for a short period. Using their formulae, the maximum possible fractional luminosity of the warm belt can be estimated as $f_{max} = 0.16 \times 10^{-3} R_{bb,w} M_*^{-5/6} L_*^{-1/2} t_{age}^{-1}$, where the radius of the belt ($R_{bb,w}$), stellar mass, luminosity and age (M_* , L_* , t_{age}) were taken from Tables 5 and 2. We found that the measured fractional luminosities ($f_{d,w}$) are always less than $0.1 f_{max}$. Therefore no transient events have to be invoked to explain the amount of observed warm dust, and a steady-state evolution of an inner planetesimal belt can be consistent with the observations. The fractional luminosity of the cold disc component ($f_{d,c}$) exceeds the fractional luminosity measured for the warm component of the same system ($f_{d,w}$) by a factor of four at least. Since the relative dust masses in the inner and outer dust belts are proportional to $\propto f_d R_d^2$ (Wyatt 2008), the difference is even significantly higher in terms of dust mass.

Basic characteristics of the outer cold belts. The characteristic temperatures of the cold outer belts in our targets are in most cases well within the range found for large samples of cold debris discs (Ballering et al. 2013;

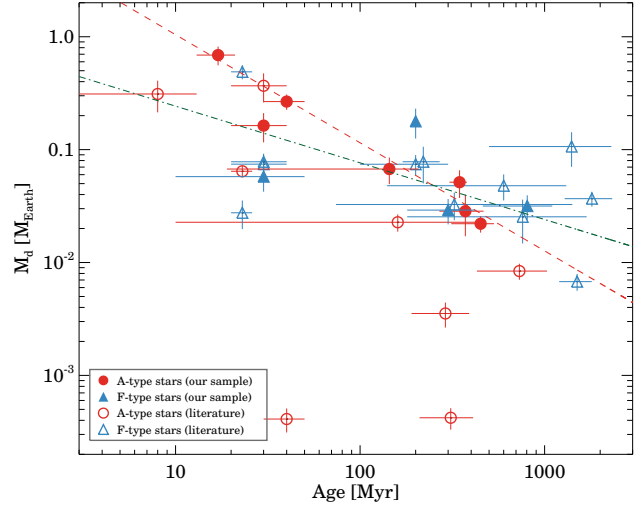


Figure 5. Measured dust masses as a function of age for our discs and for other debris systems detected at submillimetre/millimetre wavelengths. Literature data are from the following sources: Sheret, Dent, & Wyatt (2004); Najita & Williams (2005); Williams & Andrews (2006); Nilsson et al. (2009, 2010); Churcher et al. (2011); Kennedy et al. (2012a); Meeus et al. (2012); Booth et al. (2013); Eiroa et al. (2013); Panić et al. (2013). The red dashed line shows our fit to the upper envelope of data points corresponding to A-type stars. Our fitting to the whole sample are displayed by a green dashed-dotted line.

Chen et al. 2014). The only exception is HD 170773, which is one of the coldest known debris discs with its $T_{bb,c} = 37$ K. The derived β values range between 0.4 and 1.2, consistently with earlier results indicating that more processed debris dust grains typically have β values between 0 and 1.2 (e.g. Roccatagliata et al. 2009; Nilsson et al. 2010; Booth et al. 2013), as opposed to the $\beta \sim 2$ of interstellar dust grains (Li & Draine 2001). The λ_0 parameter is related to characteristic grain radius in the disc (e.g., Backman & Paresce 1993). For our sample λ_0 is between 35 and 135 μm , in most cases the obtained parameter is close to 100 μm , a typical value in debris discs (Williams & Andrews 2006). Thus, although due to our selection criteria, our sample represents unusually large, extended structures, the properties of dust grains seem to be very similar to those in smaller, more typical debris discs.

Evolution of dust mass. In Figure 5 we plotted the dust masses inferred from submillimetre observations as a function of system age. For comparison, we collected additional submillimetre/millimetre detections for debris discs around A- and F-type stars from the literature. The dust masses of the latter systems were recalculated using the same κ_0 mass absorption coefficient and technique adopted for our targets (Sect. 4.1). We note that the dust mass estimates are usually quite uncertain because 1) the submillimetre detections have generally low signal-to-noise ratio; 2) the errors of such parameters as e.g. dust temperature, β , distance are propagated to the final uncertainty. Moreover, the mass absorption coefficient is currently not well known at submillimetre wavelengths (e.g., Nilsson et al. 2010). Figure 5 shows that nearly all of our sources are located close to the upper

envelope of the distribution, i.e. at a specific age they are among the most massive debris discs. Since the plotted data are already biased towards the most massive discs – low-mass discs can be detected only around nearby, older stars (Panić et al. 2013) – our objects belong to the top range of debris discs in terms of mass. By analyzing dust masses of debris discs around Sun-like stars, Roccatagliata et al. (2009) found a moderate correlation with age. On a larger sample, including also intermediate mass stars, Panić et al. (2013) reported that the upper envelope of the dust mass distribution remains relatively flat at all ages. Our survey provides new or improved dust mass estimates for several systems, and in particular around A-type stars. Focusing only on discs around A-type stars, the data points hint at a decrease of the upper envelope of the distribution with increasing age. Using an analytic steady state evolutionary model Wyatt et al. (2007) predicted that the decay of dust mass is inversely proportional to time ($M_{\text{dust}} \propto t^{-1}$), whereas more detailed analytic models suggest a gentler slope of $t^{-0.3\dots-0.4}$ (Löhne, Krivov, & Rodmann 2008). Modelling the collisional evolution of debris discs Gáspár, Rieke, & Balog (2013) argued that the decay rate varies with time and $M_{\text{dust}} \propto t^{-0.8}$ at the fastest point of this process. We performed a Bayesian linear regression method developed by Kelly (2007) to derive the best fit line (in log-log scale) to data points corresponding to A-type stars and obtained a slope of -0.95 ± 0.16 for the upper envelope. By fitting the whole sample including both discs around A- and F-type stars using the same method we obtained a slope of -0.50 ± 0.12 . These results are consistent with the predictions of above-mentioned models.

5.2 Location of the cold planetesimal belt

In Sect. 4.3 we used a geometrical model to estimate the apparent extent of the IR emitting region in the PACS images. For each object we calculated the weighted averages of the R_{in} , R_{avg} , and R_{out} parameters obtained in different PACS bands. The inferred averaged outer radii $\langle R_{\text{out}} \rangle$ range from 190 to 450 au (Table 6), thus these discs are significantly larger than our Kuiper-belt in which most objects are located between 39 and 48 au (Jewitt, Moro-Martín, & Lacerda 2009). The ratio of the average disc radii inferred from the IR images to the radii derived from the dust temperature assuming blackbody grains ($\Gamma = \langle R_{\text{avg}} \rangle / R_{\text{bb},c}$) is higher than 1 for all our systems, ranging between 1.1 and 3.1. It is consistent with previous results derived for other spatially resolved debris discs and can be interpreted as the signature of small, ineffectively emitting grains in the system (Booth et al. 2013; Morales et al. 2013; Rodriguez & Zuckerman 2012).

We found that the observed far-IR brightness distributions can be better fitted by broad dust rings in all of our discs. Indeed, Booth et al. (2013) also suggested that at least 4 among their 9 resolved discs are relatively broad. Such results do not inevitably mean that the parent planetesimal belt is also broad since collisional processes can naturally lead to a dust distribution more extended than the birth ring itself (Strubbe & Chiang 2006). In debris discs mutual collisions gradually grind large bodies into smaller ones that are expelled by radiation pressure, producing an outwardly extended dust population (Krivov, Löhne, & Sremčević 2006).

In principle the Poynting-Robertson (PR) drag can also contribute to a wider dust distribution by drifting grains towards the central star. However, by computing both the dust removal timescale due to PR-drag (τ_{PR} , derived using the formula of Wyatt et al. 2005a) and due to collisions (τ_{coll} , derived following Zuckerman & Song 2012) in our systems, we found that $\tau_{\text{coll}} \ll \tau_{PR}$ for all relevant grain sizes. It implies that these discs are collisionally dominated, i.e. PR drag can be neglected and the width of the dust distribution is mainly affected by processes related to the radial component of the stellar radiation pressure.

For investigating the feasibility of different stirring mechanisms in our targets, we have to estimate the location of the dust-producing planetesimals. Therefore it would be important to know how our PACS observations are affected by small grains expelled from the parent belt, i.e. how well we can trace the birth ring at these wavelengths? Those small grains where β_{gr} , the ratio of the radiation pressure to gravity forces, is higher than 0.5 are blown away on hyperbolic orbits on a short timescale, while larger grains are moved onto more eccentric orbit (Krivov, Löhne, & Sremčević 2006). It results in a radial grain size segregation beyond the parent belt. Using a numerical model, Thebault, Kral, & Augereau (2014) investigated the grain size distribution beyond a narrow birth ring of colliding planetesimals. They found that at a specific radial distance the geometrical cross section of dust is dominated by the largest grains that can reach the given region, i.e. those particles whose apoastron is located at that radial position. Because of their decreasing emissivity, grains with a size of $< \frac{\lambda}{2\pi}$ have typically little contribution to the emission observed at wavelength λ . As a consequence, at longer and longer wavelengths we can detect smaller and smaller part of these extended outskirts of dust. Using equation 19 from Burns, Lamy, & Soter (1979) we computed the β_{gr} value for an compact, spherical astrosilicate grain (Draine 2003) with a size of $\frac{70}{2\pi}$, $\frac{100}{2\pi}$, and $\frac{160}{2\pi}$ μm and with a density of 2.7 g cm^{-3} at all our targets. Assuming a narrow belt of parent bodies in circular orbit at a radial distance of r_{br} we also derived the orbital eccentricity ($e = \frac{\beta_{gr}}{1-\beta_{gr}}$) and the apoastron radial distance (r_{ap}) of these grains. We found that for eight out of our eleven objects $r_{ap}/r_{br} < 1.3$ at $100 \mu\text{m}$. For the six fainter stars this result holds also at $70 \mu\text{m}$. In the case of the three most luminous objects (HD 161868, HD 182681, and HD 10939) at 70 and $100 \mu\text{m}$ the observable region could be more extended, however at $160 \mu\text{m}$ the effectively emitting grains are also expected to be confined within $1.3r_{br}$. This suggests that even in these cases at least at $160 \mu\text{m}$ we can trace the birth ring and its immediate vicinity with a reliability of 30%.

The calculations above contain several simplifications, e.g. 1) narrow birth rings were assumed; 2) when computing the grain sizes we adopted compact homogenous spheres, while in real discs the dust particles may be porous and larger for the same β_{gr} (Kirchschlager & Wolf 2013). In order to further evaluate the possible difference between the location of dust grains effectively emitting at PACS wavelengths and the location of the parent planetesimal belt, we made an additional empirical comparison. Emission at (sub)millimetre wavelengths ($>300 \mu\text{m}$) predominantly comes from large grains with size of typically $>50 \mu\text{m}$. Such large grains are little affected by radiative forces, thus, being

close to their birth area they trace the distribution of the parent planetesimals (Thebault, Kral, & Augereau 2014). From the literature, we selected four debris discs (β Pic, HD 107146, HD 109085, HR 8799) that were resolved at millimetre wavelengths (Dent et al. 2014; Hughes et al. 2011; Wyatt et al. 2005a; Patience et al. 2011) and for which *Herschel* PACS observations are also available in the Archive and whose angular size is comparable with that of our sources. We processed the *Herschel* data with HIPE utilizing the same method, as described in Sect. 2.2.1, and then disc sizes were derived by applying our broad disc models (see Sect. 4.3). HD 21997, one of our targets was also resolved at submillimetre (Moór et al. 2013b) wavelength, thus we added it to this sample. We found the PACS-based average disc radii ($\langle R_{\text{avg}} \rangle$) always to be smaller than the outer radii measured on millimetre images.

Our theoretical considerations predict that the radius of the planetesimal belt may not differ from R_{out} by more than 30%, where R_{out} is the disc radius determined from the PACS images. Since $\langle R_{\text{avg}} \rangle$ was always found to be smaller than $\langle R_{\text{out}} \rangle / 1.5$ in our sample (Table 6), it can be considered as a lower limit for the extent of the planetesimal belt. Combining this result with our conclusions from discs resolved at submillimetre wavelengths, in the following analyses we will adopt the derived $\langle R_{\text{avg}} \rangle$ values (Table 6) as a proxy for the outer edge of the planetesimal belts.

5.3 Stirring mechanism

In the literature three different mechanisms have been invoked to explain the dynamical excitation of planetesimals in debris discs: self-stirring, planetary stirring, and stirring initiated by stellar encounters (Sect. 1). In the following, we examine which stirring scenarios could work in our disc sample.

5.3.1 Self-stirring

Using a hybrid multiannulus coagulation code, Kenyon & Bromley (2008) followed the size and orbital evolution of initially small (1 m–1 km) planetesimals in a broad belt between 30 and 150 au. In the self-stirred model, bodies of the initial planetesimal population have low random velocities, thus their collisions lead to coagulation. After certain time, the largest planetesimals start accreting smaller bodies very effectively due to gravitational focusing, resulting in their runaway growth. In this phase the system becomes more and more dominated by a few big planetesimals whose growth slows down when they become large enough to increase the velocity dispersion of neighbouring small planetesimals and thereby decreasing the gravitational focusing factor. Then the growth of the large planetesimals switches to the much slower oligarch growth stage. According to the model of Kenyon & Bromley (2008) the growing oligarchs can excite the motion of neighbouring small bodies so efficiently that their collisions produce debris instead of mergers. Once fragmentation begins, continued stirring leads to a collisional cascade, where a primordial body is ground down into smaller and smaller fragments until all its mass ends up in grains small enough to be removed from the system by radiation pressure. After

a peak in the dust production, as the cascade removes a large fraction of planetesimals from the given region, the collisions become less frequent leading to a decline in dust replenishment. Since the growth time is proportional to $\frac{P}{\Sigma}$, where P is the orbital period and Σ is the surface density, the formation of large planetesimals requires more time at larger radii, i.e. it is an inside-out process, the collisional cascade is ignited in the inner disc first and then the active dust production propagates outward. In their model, Kenyon & Bromley (2008) adopted a disc with an initial surface density distribution of

$$\Sigma(a) = \Sigma_0 (M_*) x_m (a/a_0)^{-3/2}, \quad (4)$$

where Σ_0 is the reference surface density at a radius of $a_0 = 30$ au, while x_m is a scaling factor. The reference surface density was scaled with the stellar mass as $\Sigma_0(M_*) = 0.18(M_*/M_\odot) \text{ g cm}^{-2}$ ($\Sigma_0 = 0.18 \text{ g cm}^{-2}$ corresponds to the surface density of the minimum mass solar nebula, MMSN, at the radius of 30 au). Kenyon & Bromley (2008) found that the formation of the first 1000 km icy planetesimals at a radius a occurs at:

$$t_{1000} = 145 x_m^{-1.15} (a/80 \text{ au})^3 (2M_\odot/M_*)^{3/2} [\text{Myr}]. \quad (5)$$

Thus the more massive was the disc initially the faster is the initialization of the cascade at a specific radius. Since the initial disc mass (or surface density) is limited, the front of stirring – the region where the collisional cascade is ignited at a specific age – is also limited. Adopting a protoplanetary disc with a surface density distribution of $\Sigma(a) \propto a^{-3/2}$ and with a gas-to-dust mass ratio of 100:1, Mustill & Wyatt (2009) proposed that x_m have to be < 10 since a more massive disc would become gravitational unstable at radii > 100 au. Indeed, the mass of a disc that extends from 1 au to 200 au (typical outer radius for our systems) and have a surface density ten times higher than that of MMSN would be $\sim 0.55 M_\odot$. (Sub)millimetre observations indicate that isolated Herbig Ae stars with stellar masses similar to our objects typically harbour less massive discs (Williams & Cieza 2011; Sandell, Weintraub, & Hamidouche 2011). Thus, even if we take into account the well known uncertainties in disc mass estimates (Williams & Cieza 2011), the suggested $x_{m,\text{max}} = 10$ limit seems to be rather conservative and secure.

In Figure 6 we plotted the obtained average disc radii ($\langle R_{\text{avg}} \rangle$) as a function of system age for our targets. The disc around HD 21997 was also resolved with ALMA at 886 μm , in its case we adopted the outer radius derived from the submillimetre interferometric data (Moór et al. 2013b). We also plotted two additional young debris discs around stars with masses similar to our targets: β Pic and HR 8799. β Pic belongs to the ~ 23 Myr old (Mamajek & Bell 2014) β Pic moving group, while HR 8799 is a member of the ~ 30 Myr old Columba association (Zuckerman et al. 2011), thus they have reliable age estimates. Information for the outer edges of their discs were taken from resolved images published in Dent et al. (2014); Patience et al. (2011); Matthews et al. (2014a).

Using Eqn. 5, in Figure 6 we overplotted the disc radius where 1000 km size planetary embryos has just formed, for a small grid of discs with $x_m = 1, 3, 10$ and for $M_* = 1.5, 2.0 M_\odot$. The figure suggests that the size of discs around our older targets (HD 10939, HD 17848, HD 50571,

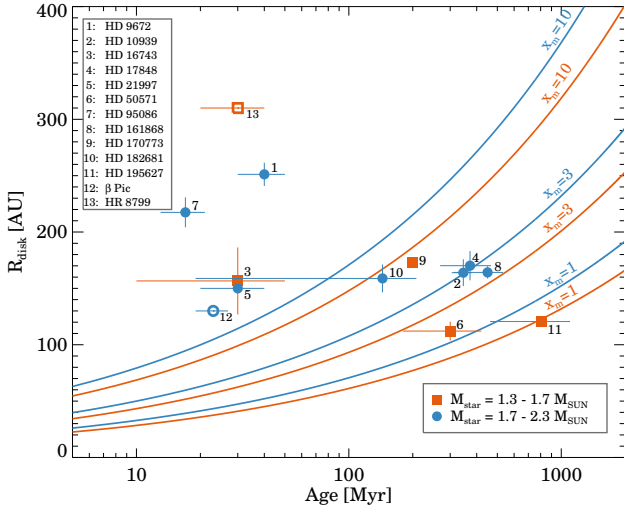


Figure 6. Derived disc radii as a function of stellar ages overplotted by self-stirring models computed for host stars with masses of 1.5 and $2.0 M_{\odot}$ (orange and blue lines) and for three different initial x_m values. Our targets are marked by filled symbols, the two additional discs are indicated by empty symbols. We note that for members of different kinematic groups, HD 9672, HD 21997, β Pic, HD 95086 and HR 8799 the age estimates are more reliable.

HD 161868, HD 170773, HD 182681 and HD 195627) can be well explained within the framework of the self-stirring model. In these cases there was enough time for the formation of large embryos even at the outer edge of the disc, and the initial surface density of the original protoplanetary disc did not exceed 10 times that of the MMSN.

The figure also suggests that the initial disc masses in our sample were rather high, in almost all cases higher than the MMSN by a factor of 1–10. This conclusion is in accordance with our earlier findings that in Figure 5 the present-day dust masses in our systems are among the most massive debris discs for their age. Large dust mass suggests a massive underlying planetesimal belt, whose formation probably required a high mass protoplanetary disc as well.

While constructing Fig. 6 we assumed that the timescale of the outward propagation is equal to the age of the system. This might not be true, however, because the expanding ring of planetesimal stirring could have reached in the meantime the outer edge of the protoplanetary disc where it stopped. The typical size of protoplanetary discs – measured from silhouettes of 22 proplyds in the Orion region – range between 50 and 200 au (Vicente & Alves 2005), very similar to the typical sizes of our debris discs. Thus, it is possible that in some of our systems the expansion of the collisional cascade has already finished some time ago, and we now observe a late phase evolution of the debris disc. Note that in this case, due to the reduced evolutionary timescale, the initial protoplanetary disc had to be even more massive than suggested in Fig. 6.

Our results do not mean that self-stirring is the only possible explanation for the seven mentioned objects in our sample. Since these discs are rather massive, giant planets might have also been formed, and they could contribute to the stirring of planetesimals (for more details see Sect. 5.3.2).

All of our objects with age ≤ 40 Myr, HD 9672, HD 16743, HD 21997, and HD 95086 as well as β Pic and HR 8799 are located above the model curves predicted by the self-stirred model, implying that they would require $x_m > x_{m,max} = 10$. Age estimates of these targets are reliable, in most cases based on moving group membership. Since the differences between the derived and predicted sizes are larger than the uncertainties related to estimates of the location of dust producing planetesimals, these objects can be considered as prime candidates where the self-stirring scenario may not work.

In order to check how robust are the conclusions concerning these debris discs, one can test how sensitive are the outcomes of the self-stirring model on its basic assumptions. Kenyon & Bromley (2010) investigated some modifications of the self-stirring model. In one, they derived an equation similar to Eqn. 5 for a disc with a flatter surface density profile. In the other, they started their simulations using uniform initial planetesimal sizes of 1 km or 10 km or 100 km instead of an ensemble of 1 m to 1 km sized bodies. In the third one, they considered different fragmentation properties of the colliding planetesimals. We recalculated the model curves in Fig. 6 considering these modifications, and found that HD 9672, HD 21997, HD 16743 and HD 95086, as well as, β Pic and HR 8799 are still outliers. In the previous analyses the initiation of dust production at a given radius was linked to the formation of ~ 1000 km size bodies. In fact, Kenyon & Bromley (2008) found that the cascade is already initiated at smaller sizes, once the largest oligarchs reach sizes of 500 km. Unfortunately, they offered no formulae for the formation of bodies smaller than 1000 km. Their Fig. 8 and 9 suggest that the outer front where the largest bodies are ~ 500 km is at most 30–40% larger than the site where 1000 km sized planetesimals are formed. Considering our conservative approach in determining the outer size of the planetesimal belt (Sect. 5.2), the above arguments probably will not change our conclusions.

The initial size distribution of the first planetesimals is very little constrained by current models in the literature (Johansen et al. 2014). The recently proposed turbulent concentration and gravitational clumping models (e.g. Johansen et al. 2007; Cuzzi, Hogan, & Shariff 2008) predict significantly larger initial planetesimal sizes (> 100 km) than the classical coagulation model utilized by Kenyon & Bromley (2008). As mentioned above, Kenyon & Bromley (2008) tested different initial planetesimal sizes, however, they used uniform size distribution and not an ensemble. Moreover, the maximum planetesimal size was only 100 km, while graviturbulent processes can produce planetesimals with a size of 1000 km or even larger bodies especially in discs with large initial mass (Johansen, Youdin, & Lithwick 2012). If the latter processes produce an ensemble of smaller planetesimals that can be stirred by the largest ones, then the collisional cascade can be started earlier than in the standard coagulation model. This phenomenon might help to produce very extended, young discs within the framework of self-stirring scenario. The detailed investigation of this case is out of the scope of the present paper.

In the following we will investigate whether alternative stirring mechanisms could explain the formation of the six outlier debris discs.

5.3.2 Planetary stirring scenario

If the debris system harbours also a stellar companion or giant planet(s) – which is not unreasonable in our massive discs – then this large body may interact with planetesimals formed in the same system. By investigating the effects of the secular perturbations of a planet on a planetesimal disc, Mustill & Wyatt (2009) found that they can drive planetesimals on new intersecting orbits, increasing the frequency and velocity of their collisions. Due to this dynamical excitation, the collisions become destructive and produce dust even at large radial distances. The planet’s secular perturbation first initiates a collisional cascade at the closest region of the planetesimal belt, but the excitation shifts to outer regions with time. Thus planetary stirring – similarly to self-stirring – is an inside-out process. Mustill & Wyatt (2009) showed that in the case of a perturber located closer to the star than the minor bodies (internal perturber), the crossing time – the time when the initially non-intersecting planetesimals’ orbits begin to cross – is

$$t_{\text{cross}} = 1.53 \times 10^3 \frac{(1 - e_{\text{pl}}^2)^{3/2}}{e_{\text{pl}}} \left(\frac{a}{10 \text{au}} \right)^{9/2} \times \left(\frac{M_*}{M_{\odot}} \right)^{1/2} \left(\frac{M_{\text{pl}}}{M_{\odot}} \right)^{-1} \left(\frac{a_{\text{pl}}}{1 \text{au}} \right)^{-3} [\text{yr}], \quad (6)$$

where a_{pl} and e_{pl} , are the semi-major axis and eccentricity of the planet’s orbit, M_{pl} is the mass of the planet, while a is the semi-major axis of the planetesimals. Depending on the planet’s orbital parameters and mass, its secular perturbation could excite planetesimal eccentricities, starting a collisional fragmentation at a given radius faster than the time needed for the growth of 1000 km size bodies. Thus, this stirring model can explain the presence of dust-producing planetesimals at large stellocentric radius even if the self-stirring scenario would require too high initial disc masses.

We used Eq. 6 to evaluate the feasibility of planetary stirring in our systems. In the calculations we used the age of the system as t_{cross} , assuming that the timescale of planet formation is negligible. Moreover, we assumed that the planet formed in situ and did not migrate during system’s lifetime. Whether in a given system the hypothetical planet can affect the planetesimals even at the observed outer disc radius via secular perturbations depends on its mass (M_{pl}), and semi-major axis (a_{pl}), and eccentricity. In our seven older systems with ages of >50 Myr, even a Jupiter-mass planet orbiting at >35 au with a moderate eccentricity of 0.1 can excite the motion of planetesimals located at $\langle R_{\text{avg}} \rangle$ via its secular perturbation. In two cases out of these seven (HD 50571 and HD 195627) the perturbing planet’s semi-major axis can be even lower, $\gtrsim 15$ au. The current high-contrast direct imaging observations are not sensitive enough to detect such a relatively low-mass planet at the given separations. These results suggest that although these seven systems can be explained via self-stirring, they can be equally well explained by the effect of a planet. Future, more refined planet search techniques will resolve this question.

For systems where the self-stirring model found to be unfeasible – HD 9672, HD 16743, HD 21997, HD 95086 from our sample and HR 8799 and β Pic – we performed a more detailed analysis regarding the planetary stirring at the

outer edge of the planetesimal belt. In Fig. 7 we plotted the necessary eccentricity values as a function of M_{pl} and a_{pl} for these systems. We assume an internal perturber, therefore a_{pl} must be smaller than the inner radius of the outer disc. For HR 8799, β Pic, and HD 21997 we used inner radii derived from resolved submillimetre images. For the other cases we used our Herschel-based geometrical model results. Since $\langle R_{\text{in}} \rangle$ was not constrained well, we explored the range of $a_{\text{pl}} < \langle R_{\text{in}} \rangle + \sigma_{\langle R_{\text{in}} \rangle}$ for these cases. When an inner belt is present we adopted its blackbody radius as a lower limit for a_{pl} , otherwise five au, the orbital radius of Jupiter was used. The figure demonstrates that in all systems there is a large variety of M_{pl} , a_{pl} pairs where a planet with a moderate eccentricity (<0.1) can stir the outer disc in less than the systems’ age. Thus, planetary stirring is a reasonable explanation for these sources. However, the planets are typically more massive than in the previous 7 cases.

Three systems (HR 8799, β Pic and HD 95086) are already known to harbour wide orbit giant planets discovered by direct imaging technique (Marois et al. 2008; Lagrange et al. 2010; Rameau et al. 2013). For these objects we overplotted the planet’s parameters in Fig. 7 with red symbols. The planet of HD 95086 has a mass of $5 \pm 2 M_{\text{J}}$ (Rameau et al. 2013) and orbital separation of ~ 62 au (computed from the projected distance, assuming that the orbital plane and the disc are coplanar), therefore it needs to have an eccentricity of $\gtrsim 0.1$ for stirring planetesimals at $\langle R_{\text{avg}} \rangle \sim 220$ au. The mass of β Pic b is in the range of 6.0–15.5 M_{J} (Bonnefoy et al. 2013), while the semi-major axis is 8–9 au and the eccentricity is <0.17 (Chauvin et al. 2012). Based on the formula of Mustill & Wyatt (2009) we found that β Pic b can force intersecting planetesimal orbits only at radial distance of ~ 90 au or less. Thus this planet alone cannot explain the presence of large dust grains at larger radii (based on ALMA data the disc outer radius is ~ 130 au, Dent et al. 2014). At HR 8799 we considered only the outermost planet in our calculations. HR 8799 b has a projected distance of ~ 68 au to the host-star, its mass is estimated to be 5–7 M_{J} (Marois et al. 2010). The inclination of the debris disc was derived to be $26 \pm 3^\circ$ based on resolved *Herschel* PACS images (Matthews et al. 2014a). Assuming the same inclination for planet’s orbit, the orbital eccentricity must be $\gtrsim 0.1$ to efficiently excite the motion of planetesimals even at ~ 310 au, the estimated outer edge of the planetesimal belt (Matthews et al. 2014a).

According to our current knowledge, among our targets only HD 16743 have stellar companions. However, these companions are very widely separated ($\sim 12\,700$ au). By computing the crossing time for the secular perturbation of these external perturbers – utilizing Eq. 16 from Mustill & Wyatt (2009) – we found that they could not have any influence on the disc around HD 16743 at a time less than the age of the system.

It should be noted that in the previous calculations we focused only on the secular perturbation caused by a possible planet or planets formed in situ. The interaction between planets and planetesimals, however, could be manifold. A migrating massive planet could sweep the planetesimals from their original orbits by gravitational perturbation, and possibly trap them in resonances (Wyatt 2008). A planet-planet scattering can either lead to a significant clearance of leftover planetesimals making the for-

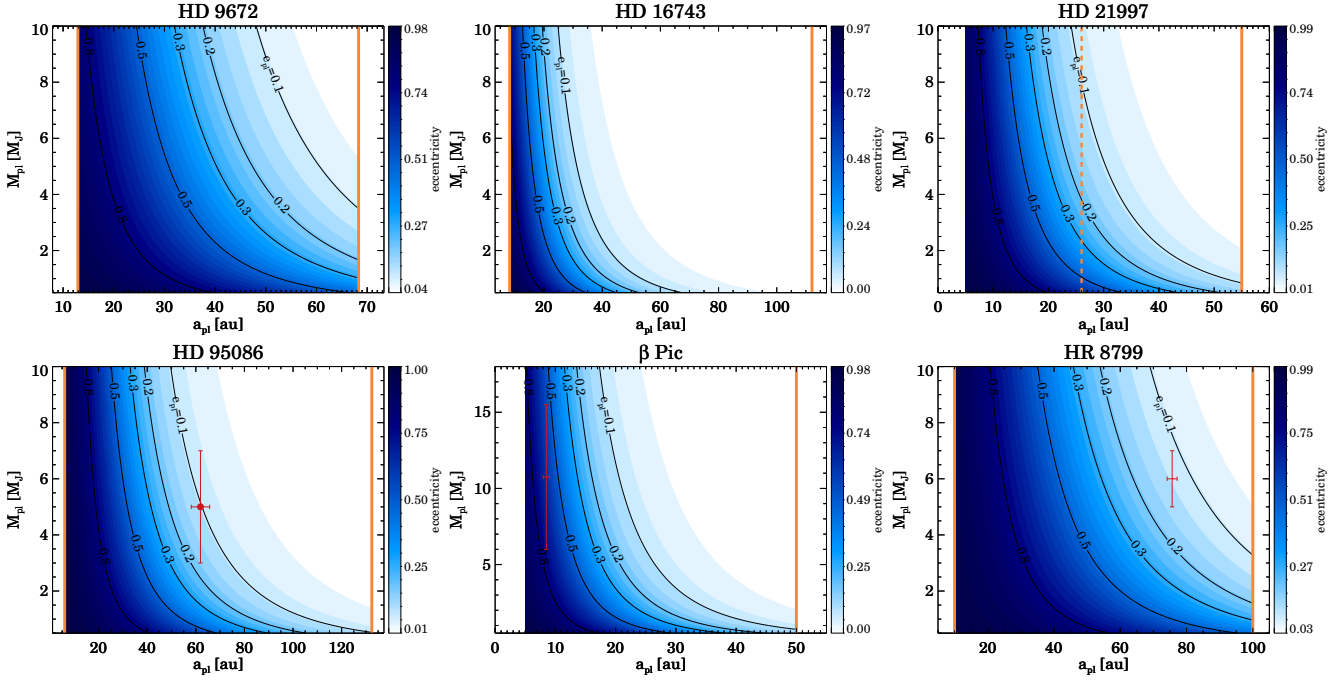


Figure 7. Evaluation of the planetary stirring model for those targets where the self-stirring model turned out to be unfeasible. The figure shows the eccentricity values, in the a_{p1}, M_{p1} parameter space, necessary to stir planetesimals located at the outer edge of the specific discs in less than the systems’ age. The black contour lines correspond to eccentricity values of 0.1, 0.2, 0.3, 0.5 and 0.8. Vertical solid lines indicate the inner radius of the outer dust belt and the radius of the inner dust belt (if it is present). For HR 8799, β Pic, and HD 21997 the inner radii of the outer component were taken from the literature (Matthews et al. 2014a; Dent et al. 2014; Moór et al. 2013b). For the other targets this parameter was set based on our geometrical models (Sect. 5.3.2). In the case of HD 21997, where gas is also present, the upper limit for the inner radius of the gas disc (taken from Kóspál et al. 2013) was also marked by a dashed orange line. There are three systems (HR 8799, β Pic, and HD 95086) where a giant planet or planets have already been discovered. In these cases the planets were also displayed by red symbols (at HR 8799, where four giant planets are known, we plotted only the outermost one).

mation of a debris disc impossible or – in case of a mild evolution – can trigger the debris formation by dynamically exciting the planetesimals (Marzari 2014). If the planetesimal population is massive enough, they also influence the dynamics of the young planet(s), either stabilizing or destabilizing the planetary system Moore & Quillen (2013). A planet formed in the inner protoplanetary disc can scatter large embryos in its neighbourhood to the outer disc (Goldreich, Lithwick, & Sari 2004), where it can excite the motion of the smaller bodies. These processes could lead the stirring of the outer planetesimals on a shorter timescale than by secular perturbation purely. Furthermore, as Mustill & Wyatt (2009) noted, their computations are valid for a system where the perturbing planet(s) and the planetesimals are far from each other. In case of close planets, the proposed formulae overestimate the crossing time. Further investigations are needed to explore the possible relevance of any of these processes for our systems.

5.3.3 Stirring induced by stellar encounters

A close encounter with a nearby star can also stir up the motion of planetesimals in the outer disc. Investigating the evolution of a planetesimal disc after a moderately close encounter with a passing star, Kenyon & Bromley (2002) concluded that such an event can raise minor bodies’ eccentricities so that collisions become destructive. However, the enhanced dust production is not maintained for a long time,

since collisions of small bodies damp the planetesimal velocities and thereby halt the collisional cascade after a time. According to Kenyon & Bromley (2002), the dust luminosity changed as $L_d/L_{bol} = L_0/[\alpha + (\frac{t}{t_d})^\beta]$, where L_0 is the maximum dust luminosity, t_d is the damping time, while values of α and β were found to be $\sim 1-2$ and ~ 1 , respectively. Discs with larger initial masses have shorter damping times and produce more dust. In a gas-free disc with a surface density corresponding to the MMSN the damping time is about 0.1 Myr at 70 au and 1.0 Myr at 140 au. If gas is also present, the damping becomes more efficient due to gas drag, resulting in shorter damping time. In the following we evaluate this scenario for our cases.

Close stellar encounters are very rare events among field stars, occurring once every 10 Gyrs (Wyatt 2008). Although close encounters are much more probable in a dense cluster (Breslau et al. 2014) none of our stars belong to such a stellar cluster now. Nevertheless, we cannot exclude the possibility that some of them were born in a dense star forming region. However, even in such a case, considering the predicted short damping timescales, an encounter-induced dynamical excitation probably does not play a crucial role in current stirring of our discs.

By tracing the space motions of more than 21000 stars in the past 1 Myr, Deltorn & Kalas (2001) investigated the possible close stellar encounters for many stars with debris discs. Interestingly, the closest encounter was found for HD 17848, one of our targets. Accord-

ing to their calculations, HD 17848 encountered with another debris-disc bearing star HD 20010 ~ 350 kyr ago with a separation of $0.081_{-0.049}^{+0.063}$ pc. Based on formulae of Kalas, Deltorn, & Larwood (2001), however, such a relatively far encounter may not have significant influence on the planetesimals motion at a stellocentric distance of $\langle R_{\text{avg}} \rangle \sim 170$ au in HD 17848. Thus, stellar encounter does not look a feasible explanation for our discs.

5.3.4 Additional considerations

HD 9672, HD 21997 and β Pic, three discs which are unlikely to be self-stirred, show another interesting feature: they are the only known debris systems where a detectable amount of CO gas was measured at molecular rotational lines (Zuckerman, Forveille, & Kastner 1995; Moór et al. 2011b; Dent et al. 2014). Depending on its quantity, the gas can have influence on the dynamics of dust grains (Takeuchi & Artymowicz 2001; Besla & Wu 2007; Krivov et al. 2009). In the β Pic system both the CO and C gas masses are lower than the measured dust mass (Dent et al. 2014; Cataldi et al. 2014). Since the gas may probably be of secondary origin (Fernández, Brandeker, & Wu 2006; Dent et al. 2014) – i.e. released from colliding/evaporating grains and planetesimals – the total gas mass may not exceed significantly the mass of these constituents and thereby the relatively low amount of gas may not have impact on the dust dynamics. Though the origin of gas in HD 9672 (49 Ceti) is still debated, recent works proposed that it may also be secondary, implying that its influence on dust might not be significant. In the disc around the ~ 30 Myr old HD 21997, we detected $0.04\text{--}0.08 M_{\oplus}$ CO gas (Kóspál et al. 2013) and argued that the gas may rather be residual primordial implying that a significant amount of H_2 gas may also be present there, thus the gas mass surpasses the dust mass. In such an environment, the gas–dust coupling could be stronger and might induce radial migration of grains whose rate depends on the amount of gas (Moór et al. 2013b). Kenyon & Bromley (2008) start their simulations in a disc where gas is also present. The gas density declines exponentially with time, the gas removal timescale was set to 10 Myr. The fact that HD 21997 still harbours large amounts of gas may significantly modify the predictions of the self-stirred model, making the analysis of stirring mechanisms difficult in this system.

Alternatively, in the youngest systems from our sample, the outermost portion of the discs can partly be composed of primordial dust grains, because without effective stirring, the low velocity collisions lead to merging, rather than destruction. In the self-stirring model, this would mean that the largest planetesimals in these outer regions are in a pre-oligarchy phase and still growing, the collisional cascade has not yet been initiated, and the bulk of available solids are in moderately large grains that are still observable at far-IR and submillimetre wavelengths. According to Heng & Tremaine (2010) and Krivov et al. (2013) in a disc where the collisions are not typically destructive, the majority of grains would radiate like blackbodies. The fact that the SED of most targets deviate significantly from a blackbody at long wavelengths ($\beta = 0.8\text{--}1.2$) and that the Γ factor is >1.0 , i.e. a significant amount of non-blackbody

grains are also present (see also in, Pawellek et al. 2014), makes this scenario less likely. Nevertheless, we cannot exclude the possibility that the outermost regions in our targets are partly composed of primordial grains. High spatial resolution multiwavelength ALMA observations will answer this question.

Interestingly, HR 8799 and HD 95086 – two discs among the three that mostly deviate from the predictions of self-stirring mode – resemble each other in terms of the structure of their planetary system as well: they harbour a warm inner dust belt and a very broad colder outer disc and giant planet(s) between the two dusty regions. Indeed, Su et al. (2013) proposed that a warm and cold debris dust belt with a large gap between them could be a signature of planets in the intervening zone. The failure of the self-stirring model could be another hint for the presence of massive planets in debris systems. Therefore HD 9672 and HD 16743, where the self-stirring was also found to be unfeasible and that may harbour multiple dust rings could also be promising candidates for planet searching programmes.

6 SUMMARY AND CONCLUSIONS

With the aim of investigating the possible stirring mechanisms in debris discs, we observed 11 targets with the *Herschel Space Observatory* between 70 and $500 \mu\text{m}$. The discs are among the most massive and extended known debris discs. The analysis of the excess emission over the photosphere implied that all targets harbour cold outer dust belts, while seven of them may also harbour warmer, inner debris dust as well. We found that all outer discs are spatially extended at 70 and $100 \mu\text{m}$, five of them being resolved for the first time.

By fitting a geometrical ring model to the far-infrared images, we determined the inclination and position angle of the discs and estimated the outer size of emitting regions, which is typically larger than 190 au. In all systems, the best fit to the observed far-IR brightness distribution was achieved by broad dust rings ($dR/R > 1$). In the case of HD 170773 even the inner edge of the disc was well resolved, revealing a broad outer dust belt between 80 and 270 au.

In order to learn about the relative importance of the possible mechanisms which may stir up the planetesimals and trigger debris dust production, we evaluated the feasibility of the self-stirring scenario for our 11 targets. To this end, we took into account their measured disc sizes and the ages of the systems and compared them to the Kenyon & Bromley (2008) model predictions. We concluded that this explanation might work for seven discs, but is highly unlikely for HD 9672, HD 16743, HD 21997 and HD 95086. In the latter young systems the dust producing regions are located far beyond the maximum stellocentric distances predicted by the self-stirring model. Using literature data, we claim that self-stirring is also unfeasible in the well-known young massive debris discs β Pic and HR 8799. Taking into account different initial planetesimal size distributions (e.g. due to rapid planetesimal formation via turbulent concentration and gravitational clumping, Johansen et al. 2014) might further refine our conclusions.

The mentioned discs are potential candidates for planetary stirring, since in all of these systems there exist

reasonable planetary configurations in which the stirring of the outer disc can be occurred. β Pic, HR 8799 and HD 95086 have already been known to harbour massive wide-separation planet(s) and in the latter two cases the known outer planets of the system can dynamically excite planetesimals in the whole disc. The other three systems, HD 9672, HD 16743, and also HD 21997, could be prime targets for future planet search programmes. Interestingly the discs around HD 9672, HD 21997 and β Pic – uniquely among known debris systems – harbour detectable amount of molecular CO gas as well.

Our study demonstrated that among the largest and most massive debris discs self-stirring may not be the only active scenario, and potentially planetary stirring is responsible for destructive collisions and debris dust production in a number of systems.

ACKNOWLEDGEMENTS

We are grateful to our referee for the useful comments. This work was supported by the Momentum grant of the MTA CSFK Lendület Disk Research Group, the ESA PECS Contract No. 4000110889/14/NL/NDe as well as the Hungarian Research Fund OTKA grants K101393 and K104607. A. M. and Gy. M. Sz. acknowledges support from the Bolyai Research Fellowship of the Hungarian Academy of Sciences. This publication makes use of data products from the Wide-field Infrared Survey Explorer, which is a joint project of the University of California, Los Angeles, and the Jet Propulsion Laboratory/California Institute of Technology, funded by the National Aeronautics and Space Administration. The publication also makes use of data products from the Two Micron All Sky Survey, which is a joint project of the University of Massachusetts and the Infrared Processing and Analysis Center/California Institute of Technology, funded by the National Aeronautics and Space Administration and the National Science Foundation. Our research has made use of the VizieR catalogue access tool, CDS, Strasbourg, France.

REFERENCES

- Abt H. A., Levato H., Grosso M., 2002, *ApJ*, 573, 359
 Backman D. E., Paresce F., 1993, in Levy E. H., Lunine J. I., eds, *Protostars and Planets III*. Univ. Arizona Press, Tucson, p. 1253
 Ballering N. P., Rieke G. H., Su K. Y. L., Montiel E., 2013, *ApJ*, 775, 55
 Balog Z., et al., 2013, *ExA*, 38
 Bendo G. J., et al., 2013, *MNRAS*, 433, 3062
 Besla G., Wu Y., 2007, *ApJ*, 655, 528
 Bonnefoy M., et al., 2013, *A&A*, 555, A107
 Bonsor A., Kennedy G. M., Crepp J. R., Johnson J. A., Wyatt M. C., Sibthorpe B., Su K. Y. L., 2013, *MNRAS*, 431, 3025
 Booth M., et al., 2013, *MNRAS*, 428, 1263
 Breslau A., Steinhausen M., Vincke K., Pfalzner S., 2014, *A&A*, 565, A130
 Burnham, K. P., & Anderson, D. R. 2002, *Model Selection and Multimodel Inference: A Practical Information-Theoretical Approach.*, by Kenneth P. Burnham, David R. Anderson, 2d ed. New York: Springer-Verlag.
 Burns J. A., Lamy P. L., Soter S., 1979, *Icar*, 40, 1
 Casagrande L., Schönrich R., Asplund M., Cassisi S., Ramírez I., Meléndez J., Bensby T., Feltzing S., 2011, *A&A*, 530, A138
 Castelli F., Kurucz R. L., 2003, *IAUS*, 210, 20P
 Cataldi G., et al., 2014, *A&A*, 563, A66
 Chauvin G., et al., 2012, *A&A*, 542, A41
 Chen C. H., Mittal T., Kuchner M., Forrest W. J., Lisse C. M., Manoj P., Sargent B. A., Watson D. M., 2014, *ApJS*, 211, 25
 Churcher L. J., et al., 2011, *MNRAS*, 417, 1715
 Crawford D. L., 1979, *AJ*, 84, 1858
 Crawford D. L., 1975, *AJ*, 80, 955
 Cutri R. M., et al., 2003, *yCat*, 2246, 0
 Cuzzi J. N., Hogan R. C., Shariff K., 2008, *ApJ*, 687, 1432
 Díaz C. G., González J. F., Levato H., Grosso M., 2011, *A&A*, 531, A143
 Deltorn J.-M., Kalas P., 2001, *ASPC*, 244, 227
 Dent W. R. F., et al., 2014, *Sci*, 343, 1490
 de Zeeuw P. T., Hoogerwerf R., de Bruijne J. H. J., Brown A. G. A., Blaauw A., 1999, *AJ*, 117, 354
 Draine B. T., 2003, *ApJ*, 598, 1017
 Eiroa C., et al., 2013, *A&A*, 555, A11
 Erspamer D., North P., 2003, *A&A*, 398, 1121
 Fernández R., Brandeker A., Wu Y., 2006, *ApJ*, 643, 509
 Gáspár A., Rieke G. H., Balog Z., 2013, *ApJ*, 768, 25
 Głębocki R., Gnaniński P., 2005, *ESASP*, 560, 571
 Goldreich P., Lithwick Y., Sari R., 2004, *ApJ*, 614, 497
 Gordon K. D., et al., 2007, *PASP*, 119, 1019
 Gray R. O., Corbally C. J., Garrison R. F., McFadden M. T., Bubar E. J., McGahee C. E., O'Donoghue A. A., Knox E. R., 2006, *AJ*, 132, 161
 Gray R. O., Corbally C. J., Garrison R. F., McFadden M. T., Robinson P. E., 2003, *AJ*, 126, 2048
 Griffin M. J., et al., 2010, *A&A*, 518, L3
 Halbwachs J. L., 1983, *A&A*, 128, 399
 Hauck B., Mermilliod M., 1998, *A&AS*, 129, 431
 Heng K., Tremaine S., 2010, *MNRAS*, 401, 867
 Høg E., et al., 2000, *A&A*, 357, 367
 Houck J. R., et al., 2004, *ApJS*, 154, 18
 Hughes A. M., Wilner D. J., Andrews S. M., Williams J. P., Su K. Y. L., Murray-Clay R. A., Qi C., 2011, *ApJ*, 740, 38
 Ishihara D., et al., 2010, *A&A*, 514, A1
 Jewitt D., Moro-Martín A., Lacerda P., 2009, *Astrophysics in the Next Decade, Astrophysics and Space Science Proceedings*, 53
 Johansen A., Oishi J. S., Mac Low M.-M., Klahr H., Henning T., Youdin A., 2007, *Natur*, 448, 1022
 Johansen A., Youdin A. N., Lithwick Y., 2012, *A&A*, 537, A125
 Johansen A., Blum J., Tanaka H., Ormel C., Bizzarro M., Rickman H., 2014, *arXiv*, arXiv:1402.1344
 Kalas P., Deltorn J.-M., Larwood J., 2001, *ApJ*, 553, 410
 Kaufer A., Stahl O., Tubbesing S., Nørregaard P., Avila G., Francois P., Pasquini L., Pizzella A., 1999, *Msngr*, 95, 8
 Kelly B. C., 2007, *ApJ*, 665, 1489
 Kennedy G. M., Wyatt M. C., 2010, *MNRAS*, 405, 1253
 Kennedy G. M., et al., 2012a, *MNRAS*, 421, 2264

- Kennedy G. M., Wyatt M. C., Sibthorpe B., Phillips N. M., Matthews B. C., Greaves J. S., 2012b, *MNRAS*, 426, 2115
- Kennedy G. M., Wyatt M. C., 2014, *MNRAS*, 444, 3164
- Kenyon S. J., Bromley B. C., 2002, *AJ*, 123, 1757
- Kenyon S. J., Bromley B. C., 2004, *AJ*, 127, 513
- Kenyon S. J., Bromley B. C., 2008, *ApJS*, 179, 451
- Kenyon S. J., Bromley B. C., 2010, *ApJS*, 188, 242
- Kirchschrager F., Wolf S., 2013, *A&A*, 552, A54
- Kóspál Á., et al., 2013, *ApJ*, 776, 77
- Krivov A. V., Löhne T., Sremčević M., 2006, *A&A*, 455, 509
- Krivov A. V., Herrmann F., Brandeker A., Thébault P., 2009, *A&A*, 507, 1503
- Krivov A. V., 2010, *RAA*, 10, 383
- Krivov A. V., et al., 2013, *ApJ*, 772, 32
- Lagrange A.-M., et al., 2010, *Sci*, 329, 57
- Lallement R., Vergely J.-L., Valette B., Puspitarini L., Eyer L., Casagrande L., 2014, *A&A*, 561, A91
- Lebouteiller V., Barry D. J., Spoon H. W. W., Bernard-Salas J., Sloan G. C., Houck J. R., Weedman D. W., 2011, *ApJS*, 196, 8
- Li A., Draine B. T., 2001, *ApJ*, 554, 778
- Löhne T., Krivov A. V., Rodmann J., 2008, *ApJ*, 673, 1123
- Makovoz D., Marleau F. R., 2005, *PASP*, 117, 1113
- Malo L., Doyon R., Lafrenière D., Artigau É., Gagné J., Baron F., Riedel A., 2013, *ApJ*, 762, 88
- Mamajek E. E., Bell C. P. M., 2014, *MNRAS*, 445, 2169
- Markwardt C. B., 2009, *ASPC*, 411, 251
- Marois C., Macintosh B., Barman T., Zuckerman B., Song I., Patience J., Lafrenière D., Doyon R., 2008, *Sci*, 322, 1348
- Marois C., Zuckerman B., Konopacky Q. M., Macintosh B., Barman T., 2010, *Natur*, 468, 1080
- Marshall J. P., et al., 2011, *A&A*, 529, A117
- Marshall J. P., et al., 2013, *A&A*, 557, A58
- Marzari F., 2014, *MNRAS*, 444, 1419
- Matthews B., Kennedy G., Sibthorpe B., Booth M., Wyatt M., Broekhoven-Fiene H., Macintosh B., Marois C., 2014a, *ApJ*, 780, 97
- Matthews B. C., Krivov A. V., Wyatt M. C., Bryden G., Eiroa C., 2014b, In *Protostars and Planets VI* (H. Beuther, R. Klessen, C. Dullemond, and Th. Henning, Eds.), Univ. of Arizona Press, Tucson, pp. 521-544.
- Meshkat T., et al., 2013, *ApJ*, 775, L40
- Meeus G., et al., 2012, *A&A*, 544, A78
- Moór A., Ábrahám P., Derekas A., Kiss C., Kiss L. L., Apai D., Grady C., Henning T., 2006, *ApJ*, 644, 525
- Moór A., et al., 2011a, *ApJS*, 193, 4
- Moór A., et al., 2011b, *ApJ*, 740, L7
- Moór A., et al., 2013a, *ApJ*, 775, L51
- Moór A., et al., 2013b, *ApJ*, 777, L25
- Moór A., Szabó G. M., Kiss L. L., Kiss C., Ábrahám P., Szulágyi J., Kóspál Á., Szalai T., 2013c, *MNRAS*, 435, 1376
- Moore A., Quillen A. C., 2013, *MNRAS*, 430, 320
- Montesinos B., Eiroa C., Mora A., Merín B., 2009, *A&A*, 495, 901
- Morales F. Y., Bryden G., Werner M. W., Stapelfeldt K. R., 2013, *ApJ*, 776, 111
- Munari U., Sordo R., Castelli F., Zwitter T., 2005, *A&A*, 442, 1127
- Mustill A. J., Wyatt M. C., 2009, *MNRAS*, 399, 1403
- Najita J., Williams J. P., 2005, *ApJ*, 635, 625
- Nielsen E. L., et al., 2013, *ApJ*, 776, 4
- Nilsson R., Liseau R., Brandeker A., Olofsson G., Risacher C., Fridlund M., Pilbratt G., 2009, *A&A*, 508, 1057
- Nilsson R., et al., 2010, *A&A*, 518, A40
- Nordström B., et al., 2004, *A&A*, 418, 989
- Olsen E. H., 1984, *A&AS*, 57, 443
- Ott S., 2010, *ASPC*, 434, 139
- Panić O., et al., 2013, *MNRAS*, 435, 1037
- Patience J., et al., 2011, *A&A*, 531, L17
- Pawellek N., Krivov A. V., Marshall J. P., Montesinos B., Ábrahám P., Moór A., Bryden G., Eiroa C., 2014, *ApJ*, 792, 65
- Perryman M. A. C., 1997, *ESASP*, 402, 1
- Pilbratt G. L., et al., 2010, *A&A*, 518, L1
- Poglitsch A., et al., 2010, *A&A*, 518, L2
- Rameau J., et al., 2013, *ApJ*, 779, L26
- Reis W., Corradi W., de Avillez M. A., Santos F. P., 2011, *ApJ*, 734, 8
- Rhee J. H., Song I., Zuckerman B., McElwain M., 2007, *ApJ*, 660, 1556
- Rieke G. H., et al., 2004, *ApJS*, 154, 25
- Roberge A., et al., 2013, *ApJ*, 771, 69
- Roccatagliata V., Henning T., Wolf S., Rodmann J., Corder S., Carpenter J. M., Meyer M. R., Dowell D., 2009, *A&A*, 497, 409
- Rodriguez D. R., Zuckerman B., 2012, *ApJ*, 745, 147
- Roussel H., 2013, *PASP*, 125, 1126
- Royer F., Zorec J., Gómez A. E., 2007, *A&A*, 463, 671
- Sandell G., Weintraub D. A., Hamidouche M., 2011, *ApJ*, 727, 26
- Sheret I., Dent W. R. F., Wyatt M. C., 2004, *MNRAS*, 348, 1282
- Shkolnik E. L., Anglada-Escudé G., Liu M. C., Bowler B. P., Weinberger A. J., Boss A. P., Reid I. N., Tamura M., 2012, *ApJ*, 758, 56
- Siess L., Dufour E., Forestini M., 2000, *A&A*, 358, 593
- Soubiran C., Le Campion J.-F., Cayrel de Strobel G., Caillo A., 2010, *A&A*, 515, A111
- Stark C. C., Schneider G., Weinberger A. J., Debes J. H., Grady C. A., Jang-Condell H., Kuchner M. J., 2014, *ApJ*, 789, 58
- Strubbe L. E., Chiang E. I., 2006, *ApJ*, 648, 652
- Su K. Y. L., Rieke G. H., Stapelfeldt K. R., Smith P. S., Bryden G., Chen C. H., Trilling D. E., 2008, *ApJ*, 679, L125
- Su K. Y. L., et al., 2013, *ApJ*, 763, 118
- Takeuchi T., Artymowicz P., 2001, *ApJ*, 557, 990
- Telesco C. M., et al., 2005, *Natur*, 433, 133
- Thebault P., Kral Q., Augereau J.-C., 2014, *A&A*, 561, A16
- Tokovinin A., Lépine S., 2012, *AJ*, 144, 102
- Torres C. A. O., Quast G. R., Melo C. H. F., Sterzik M. F., 2008, *hsf2.book*, 757
- van Leeuwen F., 2007, *ASSL*, 350,
- Vicente S. M., Alves J., 2005, *A&A*, 441, 195
- Wahhaj Z., Koerner D. W., Sargent A. I., 2007, *ApJ*, 661, 368
- Werner M. W., et al., 2004, *ApJS*, 154, 1
- Williams J. P., Andrews S. M., 2006, *ApJ*, 653, 1480
- Williams J. P., Cieza L. A., 2011, *ARA&A*, 49, 67
- Wright E. L., et al., 2010, *AJ*, 140, 1868

- Wu Y., Singh H. P., Prugniel P., Gupta R., Koleva M., 2011, *A&A*, 525, A71
- Wyatt M. C., Greaves J. S., Dent W. R. F., Coulson I. M., 2005, *ApJ*, 620, 492
- Wyatt M. C., 2005, *A&A*, 440, 937
- Wyatt M. C., Smith R., Greaves J. S., Beichman C. A., Bryden G., Lisse C. M., 2007, *ApJ*, 658, 569
- Wyatt M. C., 2008, *ARA&A*, 46, 339
- Yamamura I., Makiuti S., Ikeda N., Fukuda Y., Oyabu S., Koga T., White G. J., 2010, *yCat*, 2298, 0
- Zacharias N., Finch C. T., Girard T. M., Henden A., Bartlett J. L., Monet D. G., Zacharias M. I., 2013, *AJ*, 145, 44
- Zuckerman B., Forveille T., Kastner J. H., 1995, *Natur*, 373, 494
- Zuckerman B., Rhee J. H., Song I., Bessell M. S., 2011, *ApJ*, 732, 61
- Zuckerman B., Song I., 2012, *ApJ*, 758, 77

7.6 km s^{-1} . Analysing the kinematic properties of previously identified members of young moving groups both Shkolnik et al. (2012) and Moór et al. (2013c) requested $d_{UVW} < 5 \text{ km s}^{-1}$ as a criterion for secure group membership. Thus, based on the current results HD 182681 cannot be considered as a secure member.

APPENDIX A: HD 182681 – A CANDIDATE MEMBER OF THE β PIC MOVING GROUP?

We used the BANYAN web tool (Malo et al. 2013) to perform a first evaluation of the membership probability of HD 182681 in the β Pic moving group (BPMG). Based only on the *Hipparcos* astrometric data (position, proper motion, trigonometric parallax) only, BANYAN gave a probability of 99.3% for the membership of the star. By placing HD 182681 in the colour-magnitude diagram of young moving groups constructed by Malo et al. (2013, Fig. 3), we found a good match with the locus of BPMG stars, implying that its age could be consistent that of the group. These properties make HD 182681 a potential candidate member of the group.

In order to further investigate its membership status we obtained a high-resolution optical spectrum of HD 182681 on 2011 April 16, using the Fiber-fed Extended Range Optical Spectrograph (FEROS, Kaufer et al. 1999) on the 2.2 m MPG/ESO telescope in La Silla, Chile. The “object-sky” mode was used, with one fiber positioned at the target, and the other one on the sky. The data reduction was performed with the FEROS Data Reduction System (DRS) tool implemented within ESO-MIDAS. In order to derive the radial velocity of the star, we used the IRAF FXCOR task to cross-correlate the obtained spectrum with a synthetic template ($T_{\text{eff}}=9750 \text{ K}$, $[\text{Fe}/\text{H}]=0$, $\log g = 4.0$) from the spectral library of Munari et al. (2005). This procedure yielded a heliocentric radial velocity of $-2 \pm 10 \text{ km s}^{-1}$. The large uncertainty is due to the high projected rotational velocity of the star (275 km s^{-1} , Table 2). Using this new radial velocity measurement, we computed the galactic space velocities of the star, obtaining -3.7 ± 9.3 , -14.2 ± 1.5 , $-10.2 \pm 3.5 \text{ km s}^{-1}$ for the U, V, W components, respectively. While the V and W space velocity components match well the corresponding characteristic space velocities of BPMG ($V_0 = -16.25$ and $W_0 = -9.27 \text{ km s}^{-1}$, Malo et al. 2013) the U component (velocity toward the Galactic centre) deviates from that of the group ($U_0 = -10.94 \text{ km s}^{-1}$, Malo et al. 2013) although it is within the uncertainty. We obtained a velocity modulus of $d_{UVW} = \sqrt{(U - U_0)^2 + (V - V_0)^2 + (W - W_0)^2} =$